



University of Kentucky
UKnowledge

University of Kentucky Doctoral Dissertations

Graduate School

2010

PHYSICAL CONDITIONS INCLUDING MAGNETIC FIELDS IN SEVERAL STAR FORMING REGIONS OF THE GALAXY

Matt Lykins

University of Kentucky, millyki3@uky.edu

[Right click to open a feedback form in a new tab to let us know how this document benefits you.](#)

Recommended Citation

Lykins, Matt, "PHYSICAL CONDITIONS INCLUDING MAGNETIC FIELDS IN SEVERAL STAR FORMING REGIONS OF THE GALAXY" (2010). *University of Kentucky Doctoral Dissertations*. 95.
https://uknowledge.uky.edu/gradschool_diss/95

This Dissertation is brought to you for free and open access by the Graduate School at UKnowledge. It has been accepted for inclusion in University of Kentucky Doctoral Dissertations by an authorized administrator of UKnowledge. For more information, please contact UKnowledge@lsv.uky.edu.

ABSTRACT OF DISSERTATION

Matt Lykins

The Graduate School
University of Kentucky

2010

PHYSICAL CONDITIONS INCLUDING MAGNETIC FIELDS IN SEVERAL STAR
FORMING REGIONS OF THE GALAXY

ABSTRACT OF DISSERTATION

A dissertation submitted in partial fulfillment of the
requirements for the degree of Doctor of Philosophy in the
College of Arts and Sciences
at the University of Kentucky

By
Matt Lykins

Richmond, KY

Director: Doctor Thomas Troland, Professor of Physics

Lexington, KY

2010

Copyright © Matt Lykins 2010

ABSTRACT OF DISSERTATION

PHYSICAL CONDITIONS INCLUDING MAGNETIC FIELDS IN SEVERAL STAR FORMING REGIONS OF THE GALAXY

This document describes studies of two independent regions of the interstellar medium (ISM). These studies have the common element that both pertain to regions in our Galaxy that are known to be associated with present-day star formation. These studies aim to help us understand the ISM, star formation, and ultimately where we came from, since, after all, our star, the Sun, is itself the product of star formation 4.5 billion years ago. The first project measured the Zeeman Effect on the 21 cm H I absorption line in order to create a map of the line of sight magnetic fields near a star forming region called W3. From the map of the field, it was possible to create a three dimensional model of the magnetic field morphology. Also, calculating the various energies associated with W3 revealed that it is most likely in virial equilibrium, not expanding or contracting.

The second project used an instrument on the Hubble Space Telescope (HST) to measure the abundance of iron in a neutral region near the Orion Nebula called Orion's Veil. One of the goals of this project is to investigate whether solid dust grains can be destroyed by ionizing radiation by comparing the amount of solid iron in Orion's Veil to the amount in the nearby ionized regions. By measuring the depletion of iron in the neutral Veil and comparing it to the depletion of iron the H^+ regions of the Orion Nebula, it was possible to conclude that iron was not being released into the gas phase by ultraviolet photons. In addition, oscillator strengths for two Fe II transitions were measured.

KEYWORDS: Magnetic fields, Interstellar Medium,
Star Formation, Zeeman Effect,
HII Regions

Matt Lykins

4/22/2010

PHYSICAL CONDITIONS INCLUDING MAGNETIC FIELDS IN SEVERAL STAR
FORMING REGIONS OF THE GALAXY

By

Matt Lykins

Dr. Thomas H. Troland

Director of Dissertation

Dr. Joseph Brill

Director of Graduate Studies

4/22/2010

RULES FOR THE USE OF DISSERTATIONS

Unpublished dissertations submitted for the Doctor's degree and deposited in the University of Kentucky Library are as a rule open for inspection, but are to be used only with due regard to the rights of the authors. Bibliographical references may be noted, but quotations or summaries of parts may be published only with the permission of the author, and with the usual scholarly acknowledgments.

Extensive copying or publication of the dissertation in whole or in part also requires the consent of the Dean of the Graduate School of the University of Kentucky.

A library that borrows this dissertation for use by its patrons is expected to secure the signature of each user.

NAME

DATE

DISSERTATION

Matt Lykins

The Graduate School
University of Kentucky
2010

PHYSICAL CONDITIONS INCLUDING MAGNETIC FIELDS IN SEVERAL STAR
FORMING REGIONS OF THE GALAXY

DISSERTATION

A dissertation submitted in partial fulfillment of the
requirements for the degree of Doctor of Philosophy in the
College of Arts and Sciences
at the University of Kentucky

By
Matt Lykins

Richmond, KY

Director: Doctor Thomas Troland, Professor of Physics

Lexington, KY

2010

Copyright © Matt Lykins 2010

TABLE OF CONTENTS

List of Tables.....	iv
List of Figures	v
1. Chapter One: Introduction	1
2. Chapter Two: Basic Physics	4
2.1. Lorentz Force and Flux Freezing	4
2.2. Cloud Energetics and the Virial Theorem	6
2.3. The Zeeman Effect in the 21 cm HI line	8
2.4. Radiative transfer	10
2.5. Aperture Synthesis Observations	11
2.6. Other Important Quantities.....	12
3. Chapter Three: W3 Region	13
3.1. Overview of W3	13
3.2. Previous Magnetic Field Studies	16
3.3. Observations and Data Reduction	17
3.4. Results	18
3.5. Discussion	21
3.6. Model	22
3.7. Energetics	23
3.8. W3 Conclusions	24
4. Chapter Four: Orion’s Veil	25
4.1. Overview of the Orion’s Veil Region	25
4.2. Previous Magnetic Field Studies	27
4.3. Introduction to Measuring the Depletion of Iron.....	27
4.4. Observational Data.....	28
4.5. Analysis.....	30
4.5.1. Fe column densities derived from optical depth profiles.....	31
4.5.2. New oscillator strength estimates for 2234 & 2367 Å Fe II lines.....	35
4.5.3. Fe column densities and the Fe/H ratio in the Orion Veil	36
4.6. Discussion	36
4.6.1. Fe/H in the Orion Veil: Implications for grain destruction.....	36
4.6.2. Fe/H in the Orion Veil: the depletion – density relation.....	37
4.6.3. Comparisons with spectral synthesis models of the Orion region	38
4.6.4. Outlying velocity components.....	38
4.6.5. Physical nature of the outlying velocity components	39
4.7. Conclusions	41
5. Chapter Five: Conclusions.....	43
6. References.....	44
7. Vita	46

LIST OF TABLES

Table 2.1, Lorentz Force Example.....	5
Table 3.1, Observing Time and Dates for W3	18
Table 3.2, Magnetic Field Results vs. Roberts et al. (1993).....	21
Table 4.1, Properties and Calculated Values of Iron Absorption Lines	29
Table 4.2, Parameters of the velocity components	32

LIST OF FIGURES

Figure 2.1, Zeeman Effect Levels.....	8
Figure 2.2, Zeeman Effect Classical.....	9
Figure 3.1, W3 Overview.....	13
Figure 3.2, W3 Main.....	14
Figure 3.3, W3 Molecular Map.....	15
Figure 3.4, Stokes I and V.....	18
Figure 3.5, Big Continuum.....	19
Figure 3.6, Continuum Zoom.....	19
Figure 3.7, Magnetic Field 38.....	20
Figure 3.8, Magnetic Field 46.....	21
Figure 3.9, Hourglass Model.....	23
Figure 4.1, Huygens Region.....	25
Figure 4.2, Veil Diagram.....	26
Figure 4.3, Iron Absorption Lines.....	30
Figure 4.4, Optical Depth Profiles.....	33

1. Chapter One: Introduction

The most apparent objects in the night sky are stars. It is not surprising then that stars are the building blocks for how we classify large scale structure in the universe. However, it is important to remember that stars are not the only objects out there. There is matter between the stars. This matter is called the interstellar medium (ISM). The ISM is where stars are born. It is composed of clouds of various shapes, sizes, densities, and temperatures. These clouds are made of gas and dust. Most of the gas in the ISM is hydrogen. The hydrogen gas in the ISM exists in 3 different states. The coldest and densest regions of the ISM will contain molecular hydrogen, H_2 . Typical temperatures for H_2 regions are on the order of 20 K. The density in these regions can be as little as a few times 10^2 atoms per cubic centimeter, and the density ranges up to many orders of magnitude higher. For H_2 regions to exist, they must be shielded from radiation that would dissociate the molecular hydrogen. The shielding comes from interstellar dust that absorbs ultraviolet radiation from the ambient stellar radiation field. The second state of hydrogen that exists in the ISM is neutral atomic hydrogen, H^0 . These are regions where the molecular hydrogen gas has been dissociated but has not been ionized. Temperatures in these regions range from approximately 50 K to 5,000 K while the densities typically range from 0.2 to 50 atoms per cubic centimeter. The last hydrogen state is ionized hydrogen, H^+ ($H\ II$ is another common way to refer to this type of region). H^+ regions are regions where there is sufficient energy to ionize the atomic hydrogen. This energy usually comes in the form of stellar ultraviolet photons with wavelengths less than 92 nm, that is, photons capable of ionizing H^0 from the ground ($n=1$) energy level. H^+ regions are common around hot O and B type stars since these stars, owing to their high temperatures, are abundant sources of the ionizing ultraviolet photons. H^+ regions have temperatures on the order of 10,000 K.

In addition to gas, the ISM contains a significant amount of dust. Dust makes up approximately 1% of the mass of the ISM. The cores of interstellar dust grains are composed of relatively heavy elements, such as Mg, Al, Ca, and Fe, in the solid phase. The mechanisms that control grain formation, growth, and destruction are still under investigation. However, the origins of interstellar dust grains are believed to be in the atmospheres of aging, red giant stars that are losing a fraction of their masses to the ISM. The study of dust grains can reveal important characteristics about a region. By measuring the polarization of radiation emitted or absorbed by dust grains in a region of the ISM, it is possible to infer some information about the magnetic field in that region. Dust grains are also related to a property called depletion. As atoms in the gas phase of the ISM condense onto grains, they no longer absorb photons at the same energies that they did in the gas phase. This means that absorption line studies designed to detect the gas phase of iron, for instance, are likely to underestimate the number of iron atoms in that region. If we assume that every region of the ISM has approximately the same relative abundances of all elements (in the gas phase and in dust grains combined), then we can compare the relative abundances of a region in the ISM to the abundances in the Sun. The high temperatures in the Sun ensure that there are no grains, so all elements are in the gas phase and directly measurable by spectroscopic observation. The depletion of an element in a region of the ISM is the ratio of the gas phase abundance of that element

in the region of interest to the abundance of that element in the sun. (In all cases, abundances of the elements are given relative to H.) Depletion can also be thought of as a measure of the fraction of an element that has condensed into dust grains, hence, been lost to the gas phase.

The physics of the ISM is driven by the flow of energy. Gravitational energy is one of the most obvious and important energies for organizing the ISM, creating structure, and creating stars via gravitational contraction. However, there are other energies that play a part in shaping the ISM and star formation from the ISM. These other energies include thermal energy, turbulent energy, magnetic energy, and energy in the form of stellar radiation. When considering the ISM as a whole, there is a rough equipartition of these other (non-gravitational) forms of energy. These energies control the future of the ISM. If a region has a strong magnetic field and considerable thermal and turbulent energy, then it could be difficult for stars to form. In regions where gravitational energy dominates, stars can form rapidly. Further considerations regarding energies in the ISM are discussed in section 2.2.

What is the anatomy of a star forming region? A star forming region generally starts out as a giant molecular cloud (GMC). This is where stars are most likely to form since molecular clouds are cold and dense. For a section of the GMC to collapse and form a star, gravity must be allowed to gather and compress gas and dust with minimal effect by energies that oppose gravity. If a cloud has a high density and low temperature, the gravitational energy is high while the other energies mentioned above (e.g. thermal energy) are more likely to be low. It is thought that colder denser molecular gas and warmer, less dense atomic gas may be in pressure equilibrium in the ISM and may require a trigger for star formation. Examples of triggers for star formation could be a shock wave from a supernova or the collision of giant molecular clouds. Once a portion of the GMC starts to collapse, the collapsing region of gas will begin to heat up after the region becomes opaque to its own radiation. When nuclear fusion begins in the core, a star has formed. The high energy photons leaving the star will start to affect the molecular gas that surrounds it. Once sufficiently energetic photons are put into the molecular gas surround the forming star, the molecular gas will dissociate into atomic gas. The region on the face of the GMC where this atomic gas has been created and where the chemistry and energy of the region is controlled by these far ultraviolet photons is called a photon-dominated region (PDR). If the star is hot enough to emit photons with wavelengths less than 92 nm, then they will ionize the gas surrounding the star creating an H^+ region. Considering an idealized case of a star embedded in a homogeneous region of ISM, and neglecting the effects of a stellar wind, the regions of different hydrogen states will surround the newly formed star in spherical shells. The regions would exist in order of decreasing temperature as you move away from the star, H^+ region, atomic hydrogen region, and then H_2 region. Even in this idealized case, the system is not in equilibrium. Since the H^+ region is much hotter than the surrounding neutral regions, its pressure is also much higher. Therefore, the H^+ region expands into the surrounding gas. As the H^+ region expands, it will push the atomic and molecular gas with it away from the star.

This document describes studies of two independent regions of the ISM. These studies have the common element that both pertain to regions in our Galaxy that are known to be associated with present-day star formation. These studies aim help us understand the ISM, star formation, and ultimately where we came from, since, after all, our star, the Sun, is itself the product of star formation 4.5 billion years ago. The first project measures the Zeeman Effect on the 21 cm H I absorption line (from H⁰ gas) to measure the line of sight magnetic fields in a star forming region called W3 and an aims to create a three dimensional model of the magnetic field. As was mentioned above, magnetic field energy can play a big role in preventing star formation. So measuring the magnetic field strength and its morphology can help us understand the W3 region and possibly predict its fate. The second project uses an instrument on the Hubble Space Telescope (HST) to measure the abundance of iron in a neutral region near the Orion Nebula called Orion's Veil. One of the goals of this project is to investigate whether solid dust grains can be destroyed by ionizing radiation by comparing the amount of solid iron in Orion's Veil to the amount in the nearby ionized regions. As mentioned above, grain processes such as creation and destruction are still not fully understood. Measuring the depletion of iron in a neutral region and an H⁺ region should tell us if grains can be destroyed by high energy photons. But first, chapter 2 outlines the basic physics needed to understand the studies presented in chapters 3 and 4.

2. Chapter Two: Basic Physics

Magnetic fields are an important variable in star formation. Magnetic fields permeating self-gravitating clouds in the interstellar medium (ISM) can prevent the clouds from collapsing to form stars. This possibility arises owing to a dynamical connection between the ISM and the magnetic field called flux freezing. Flux freezing, in turn, results from the Lorentz force. Below, are some of the simple physical principles that account for flux freezing and related phenomena in the ISM.

2.1. Lorentz Force and Flux Freezing

The Lorentz force is the force felt by a moving charged particle due to an electric or magnetic field. If we assume that the electric field is zero, then the Lorentz force, in cgs units, is given by

$$\bar{F}_{Lorentz} = \frac{q}{c}(\bar{v} \times \bar{B}), \quad (1)$$

where q is the charge of the particle, c is the speed of light, v is the velocity and B is the magnetic field strength. It is easy to see from equation (1) that a charged particle moving through a magnetic field will experience a force perpendicular to both its velocity and the magnetic field.

If we assume that the Lorentz force is the net force on the particle, then it is possible to combine equation (1) with Newton's Second Law.

$$\bar{F}_{net} = m\bar{a} \quad (2)$$

$$\bar{F}_{net} = \bar{F}_{Lorentz} = \frac{q}{c}(\bar{v} \times \bar{B}) = m\bar{a} \quad (3)$$

Now if we assume that the velocity of the particle is perpendicular to the magnetic field, then equation (3) simplifies to

$$\frac{qvB}{c} \hat{r} = m\bar{a}, \quad (4)$$

where \hat{r} is a unit vector in the direction perpendicular to both v and B . Since the acceleration of the particle is always perpendicular to the velocity, the particle will move in a circle with gyro radius r . Therefore, it makes sense to convert equation (4) to rotational variables. Converting v and a to rotational variables reduces equation (4) to

$$\omega = \frac{qB}{mc} \quad (5)$$

and

$$r = \frac{v}{\omega} = \frac{vmc}{qB}. \quad (6)$$

To get a sense of the angular velocity, ω , and the radius of rotation, r , consider values of v and B that are typical for clouds in the ISM. The thermal speed of a proton in the ISM is $\approx 1 \text{ km s}^{-1}$ at 100 K, and the average magnetic field in the galaxy is $\approx 3 \text{ } \mu\text{G}$. Table 2.1 lists the values input into equations (5) and (6) as well as the results.

Table 2.1: Lorentz Force Example

	Proton	Electron
v (km s ⁻¹)	1	67
q (esu)	4.8×10^{-10}	-4.8×10^{-10}
B (μ G)	3	3
ω (rad s ⁻¹)	0.03	-50
r (km)	30	1.34

While the proton gyro radius seems large by distance scales of daily life, both proton and electron gyro radii are very small compared to any relevant scale size in the ISM. That is, the motions of charged particles in the ISM are constrained to move very tightly about the magnetic field lines.

One scenario by which the charged particles can have their circular path altered is through collision with other particles. The collision frequency depends upon three parameters, the density, the cross-sectional area, and the particle velocity,

$$f_{\text{collision}} = n\sigma v. \quad (7)$$

We can use typical density, area, and velocity values for star-forming regions to get a sense of how often collision might occur. For density, $10 \text{ particles cm}^{-3}$, is a typical value in the diffuse ISM. Hydrogen makes up the majority of the universe, and its cross-sectional area at the first Bohr orbit is approximately 1 Angstrom^2 or 10^{-16} cm^2 . For a cloud of 100 K, the average velocity, as before, is 1 km s^{-1} or 10^5 cm s^{-1} . Putting these values into equation (7) gives a collision frequency of 10^{-10} collisions per second or one collision every 300 years.

Compare the collision period with gyro period of the proton and electron from Table 2.1. The times for the proton and the electron to make one revolution around the magnetic field are approximately 219 seconds and 0.12 seconds respectively. If a collision occurs every 300 years, then the proton will circle the magnetic field millions of times and the electron will make billions of trips around before colliding with a hydrogen atom. It is clear that these particles are truly “frozen” to the field since collisions that disrupt the gyro motion of the charged particles occur very infrequently.

Even though the charged particles are flux frozen to the magnetic field, an interstellar cloud can still collapse. The neutral particles in the cloud are unaffected by the Lorentz force since they have no charge. The process by which the neutral particles are separated from the flux frozen charged particle by gravity is called ambipolar diffusion. However, the neutral particles do not free fall as if the magnetic field was absent. As the neutral particles fall toward the center of gravity, they collide with the flux frozen charged particles. These collisions slow the collapse of the cloud. The timescale for ambipolar diffusion is given by Spitzer (1998),

$$t_D = 5.0 \times 10^{13} \frac{n_i}{n_H} \text{ years} \quad (8)$$

where n_i is the ion number density and n_H is the overall hydrogen density. When compared to the gravitational free fall time also given by Spitzer (1998)

$$t_f = \frac{4.3 \times 10^7}{(n_H)^{1/2}} \text{ years}, \quad (9)$$

the timescale for ambipolar diffusion could be significantly longer. A typical value for the hydrogen density within a molecular cloud is 1000 particles per cubic centimeter. The ion density within a molecular cloud is on the order of 10^{-3} cm^{-3} . Evaluating equations (8) and (9) with these values gives a diffusion timescale of 5.0×10^7 years while the freefall time is 1.4×10^6 years. Since the ambipolar diffusion timescale is an order of magnitude larger than the freefall timescale, ambipolar diffusion is the dominant process. In other words, the magnetic field is a significant factor in supporting typical molecular clouds against collapse.

2.2. Cloud Energetics and the Virial Theorem

The fate of an interstellar cloud depends on forces that try to contain the cloud and forces that resist containment. Gravity and pressure (thermal and turbulent) from the surrounding area contain the cloud while the internal pressure of the cloud (thermal and turbulent) and the magnetic field resist the collapse. To determine the fate of the cloud, we need to compare the contributions from each of these containing and supporting forces. A common way of making this comparison is through the contribution each of these forces makes to the total energy of the cloud (see McKee et al 1993). Comparing the energies of the containing forces with those of the supporting forces will tell us if the cloud will collapse or not. This comparison amounts to an application of the virial theorem. The virial theorem states that for a system in equilibrium, the time-average of the total potential energy plus two times the time-average of the total kinetic energy equals zero. Changes in the ISM occur very slowly so it is reasonable to remove the time-averages from both energies. These assumptions lead to

$$2E_k + E_u = 0, \quad (10)$$

where E_k is the total kinetic energy and E_u is the total potential energy.

Now I will mathematically define each of the energies described above and then apply the virial theorem. The first of the containing forces is gravity. The gravitational energy of a spherical cloud is given by

$$E_G = \frac{3}{5} a \frac{GM^2}{R}. \quad (11)$$

The term “a” is a constant which depends on the density distribution in the cloud. For constant density, $a = 1$. If $\rho(r) \propto r^{-k}$, then $a = (1-k/3)/(1-2k/5)$. Density laws derived empirically for molecular clouds suggest $k \approx 1.6$ (Fuller & Myers, 1992), so $a \approx 1.3$. The other containing force is the force due to the pressure of the external medium. The energy of the external pressure is given by

$$E_E = 3\sigma^2 \rho_0 V_{cloud}, \quad (12)$$

where σ is the one dimensional velocity dispersion of the external medium, ρ_0 is the density of the external medium, and V_{cloud} is the volume of the cloud. The internal pressure is due to the kinetic energy from thermal and macroscopic motions (turbulence). The total internal energy (both thermal and turbulent) is given by

$$E_k = \frac{3}{2} M \sigma^2, \quad (13)$$

where σ is the one dimensional velocity dispersion of the cloud. The other supporting energy is due to the magnetic field. The magnetic field energy within a sphere of radius R is given by

$$E_B = b \frac{B^2 R^3}{3}, \quad (14)$$

where b is a constant which accounts for magnetic gradient effects. Values of b can be estimated from detailed analytical or numerical models of self-gravitating clouds connected to an external medium by a magnetic field. For example, Tomisaka et al. (1988) yield $b = 0.3$. Using the absolute values of each of the energies, they can be arranged in terms of containment versus support using the virial theorem as follows

$$E_G + E_E = 2E_K + E_B. \quad (15)$$

Dividing the right side of equation (15) by the left side leads to

$$\frac{2E_K + E_B}{E_G + E_E} = 1. \quad (16)$$

If equation (16) is equal to 1 then the cloud is stable against contraction or expansion. If this ratio is greater than 1, the cloud is unstable to expansion and if it is less than 1 the cloud is unstable to collapse.

At times, one may wish to compare gravitational and magnetic energies in a cloud. The magnetic field which causes the magnetic energy to be equal to the gravitational energy is called B_{crit} . Equating equations (11) and (14) leads to

$$B_{crit} = \sqrt{\frac{9aGM^2}{5bR^4}}. \quad (17)$$

Another common way to quantify the relation ship between magnetic field energy and gravitational energy is with λ , used by Crutcher (1999). λ is the ratio of the mass to flux ratio of the cloud to the critical mass to flux ratio,

$$\lambda = \frac{\frac{M}{\Phi_B}}{\left(\frac{M}{\Phi_B}\right)_{crit}}. \quad (18)$$

The critical mass to flux ratio can be found by equating equations (11) and (14),

$$\frac{3}{5} a \frac{GM^2}{R} = b \frac{B^2 R^3}{3}. \quad (19)$$

Solving equation (19) for mass divided by magnetic flux yields

$$\left(\frac{M}{\Phi_B}\right)_{crit} = \frac{M}{BR^2} = \sqrt{\frac{5b}{9aG}}. \quad (20)$$

If $\lambda < 1$ then the cloud is said to be magnetically subcritical, and it cannot collapse regardless of the external pressure. If $\lambda > 1$ then the magnetic field permeating the cloud is not strong enough to support it. The cloud is said to be magnetically supercritical and will collapse unless it is supported by internal motions. Also, it can easily be shown that λ^2 is equal to the ratio of the gravitational energy, equation (11), and the magnetic energy, equation (14).

2.3. The Zeeman Effect in the 21 cm HI line

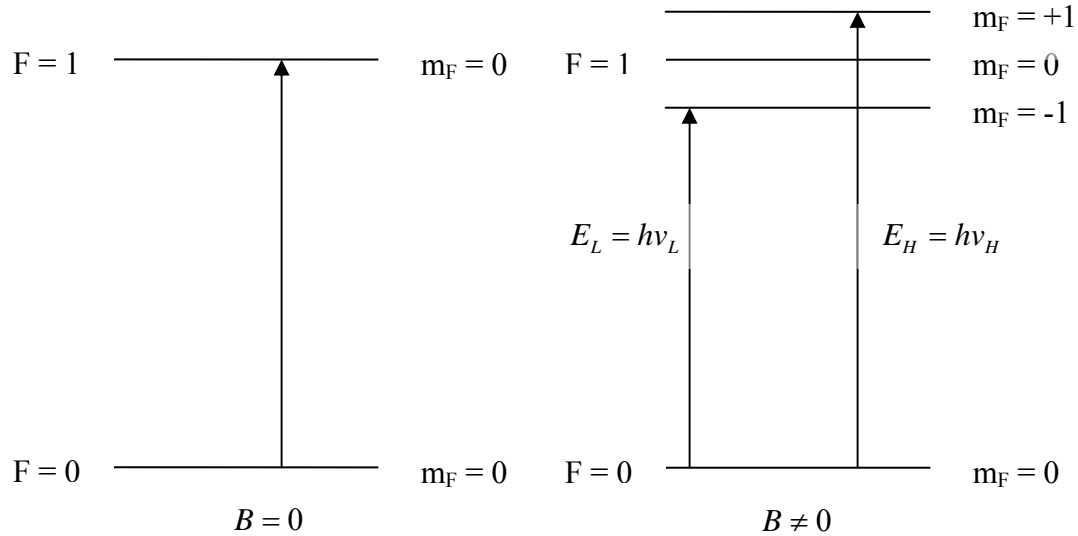


Figure 2.1: The interaction between the electron and nuclear spins in the hydrogen atom give rise to hyperfine energy levels. The figure on the left illustrates a transition from the lowest hyperfine level to the next lowest. The figure on the right shows how these hyperfine levels are split in the presence of a magnetic field due to the Zeeman Effect.

The Zeeman Effect is the splitting of atomic energy levels in the presence of an external magnetic field. For example, consider the 21 cm H I transition. Figure 2.1 (left) shows the hyperfine energy level diagram for that transition when no external magnetic field is present. Figure 2.1 (right) shows the hyperfine energy level diagram when a magnetic field is applied. The $F=1$ state is split into 3 different sub-states with different energies. The new energy levels are separated from $m_F=0$ by,

$$\Delta E = h(\nu_H - \nu_L) \quad (21)$$

where ν_H is the frequency of the photon absorbed to get to the higher energy state, while ν_L is for the lower state. ΔE is proportional to the strength of the external magnetic field which caused the splitting. The separation may also be described in terms of wavelength, $\Delta\lambda$, or frequency, $\Delta\nu$.

The frequency separation per unit magnetic field strength can be calculated using classical physics. Consider three oscillating electrons under the influence of an unspecified central force, shown in Figure 2.2. Electron 1 oscillates along the z-axis through the origin, electron 2 revolves around the z-axis counter-clockwise, and electron 3 revolves around the z-axis clockwise. The angular velocity, ω_0 , of the electrons can be found using

$$F_{central} = m\omega_0^2 r. \quad (22)$$

Now, let's add a constant uniform magnetic field along the z-axis. How does the oscillation frequency of each electron change with the added field? The new angular

velocity can be found by adding the forces. The Lorentz force, equation (1), does not affect electron 1 because its velocity is parallel to the magnetic field. Therefore, the net force on electron 1 is the central force F_{central} . That means that the angular velocity is unchanged with the addition of the magnetic field. In other words, the oscillation frequency remains the same. Electrons 2 and 3 are affected by the Lorentz force since their velocities are always perpendicular to the magnetic field. The new angular velocity for electron 2 is given by

$$m\omega'^2 r = m\omega_0^2 r - \frac{evB}{c}. \quad (23)$$

In equation (23), I have added the Lorentz force, equation (1), for an electron with a velocity that is perpendicular to the magnetic field to the original central force. The Lorentz force term is negative because the direction of the force is away from the center of revolution. The equation for electron 3 is identical except that the Lorentz force term is positive. Solving for ω' , adding consideration for electron 3, and converting to angular units leads to

$$\omega' = \sqrt{\omega_0^2 \pm \frac{e\omega_0 B}{mc}}. \quad (24)$$

Assuming $\frac{eB}{mc} \ll \omega_0$, equation (24) reduces to,

$$\omega' = \omega_0 \pm \frac{eB}{2mc} \quad (25)$$

via binomial expansion. Converting equation (25) to frequency is a simple matter, which leads to

$$\nu' = \nu_0 \pm 1.40 \frac{\text{Hz}}{\mu\text{G}}. \quad (26)$$

The frequency separation per magnetic field is $1.40 \text{ Hz } \mu\text{G}^{-1}$. It is easy to see then that electron 3 represents the transition E_H in Figure 2.1, while electron 2 represents E_L .

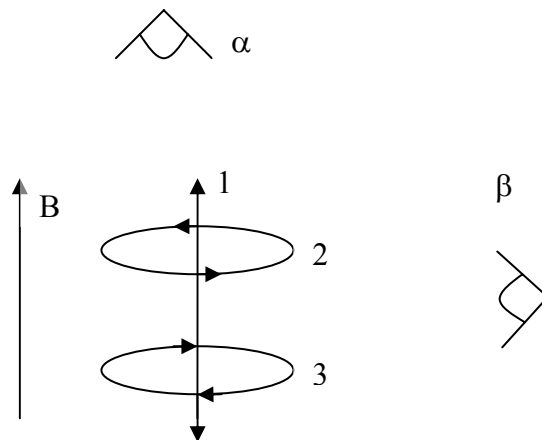


Figure 2.2: This is a classical diagram used to illustrate the Zeeman Effect. There are 3 oscillating charged particles in a magnetic field viewed from two different perspectives.

This simple classical model of 3 oscillating electrons can also explain the observed polarizations of the light emitted or absorbed when the Zeeman Effect is present. The sense of polarization that an observer detects depends on the orientation of the magnetic field relative to the observer. Observer α , with the magnetic field along the line of sight, detects the emission from electron 2 as right-circularly polarized (RCP) light. Electron 3 shows left-circular polarization (LCP) and electron 1 is not detected. By equation (26), the frequency separation of the RCP and LCP is $2.8 \text{ Hz } \mu\text{G}^{-1}$. By measuring the frequency separation between RCP and LCP, it is possible to make an estimate of the line of sight component of the magnetic field causing the splitting. Observer β has the magnetic field completely in the plane of the sky. Electrons 1, 2, and 3 are all detected as producing linear polarizations. If observer β sees the light emitted from electron 1 as horizontal linear polarization, then light from electrons 2 and 3 will be detected as vertical linear polarization. Estimates of the plane of the sky component of the magnetic field using linear polarization are not currently possible. The reason is that the emissions or absorptions from electrons 2 and 3 have the same sense of linear polarization. Having the same sense of polarization and a small frequency separation makes the emission or absorption lines from electrons 2 and 3 indistinguishable.

2.4. Radiative transfer

Radiative transfer is the physical process which describes how electromagnetic radiation interacts with matter. Imagine photons from a background source of radiation propagating through a medium on their way to the observer. The medium both absorbs and emits radiation. The equation of radiative transfer,

$$\frac{dI_\nu}{ds} = -k_\nu I_\nu + j_\nu, \quad (27)$$

describes how photons are absorbed, emitted, or scattered when interacting with matter. In equation (27), I_ν is the specific intensity, s is the path length through the medium, k_ν is the absorption coefficient, and j_ν is the emission coefficient. To solve equation (27) we define a quantity called optical depth. Optical depth is a measure of the amount of radiation removed from a beam as it passes through a medium. The optical depth is zero at the edge of the medium closest to the observer and gets larger as you move toward the radiation source. The equation for optical depth is given by

$$d\tau_\nu = -k_\nu ds \quad (28)$$

If we assume that the medium has an optical depth of τ_{Tot} , then the solution to equation (27) is

$$I_\nu = I_\nu(0)e^{-\tau_{\text{Tot}}} + \int_0^{\tau_{\text{Tot}}} \frac{j_\nu}{k_\nu} e^{-\tau_\nu} d\tau_\nu, \quad (29)$$

where $I_\nu(0)$ is the specific intensity on the source-side of the medium. If we consider the medium to be in thermodynamic equilibrium, then the specific intensity is the Planck function,

$$B_\nu = \frac{2h\nu^3}{c^2} \frac{1}{e^{h\nu/kT} - 1}, \quad (30)$$

and the derivative of it with respect to distance is zero. Combining these two facts with equation (27) yields

$$B_\nu = \frac{j_\nu}{k_\nu}. \quad (31)$$

Combining equations (29) and (31) gives

$$I_\nu = I_\nu(0)e^{-\tau_{tot}} + B_\nu(T)\{1 - e^{-\tau_{tot}}\} \quad (32)$$

For radio wavelengths, it is common for $h\nu/kT$ to be much less than unity which allows equation (30) to be approximated by the Rayleigh-Jeans law,

$$B_\nu = \frac{2\nu^2 kT}{c^2}. \quad (33)$$

It is common to express specific intensity as brightness temperature, T_b . The brightness temperature is the temperature at which $B_\nu(T_b)$ is equal to the specific intensity, I_ν .

Expressing equation (32) in terms of brightness temperature leads to

$$T_b = T_b(0)e^{-\tau_{tot}} + T_{ex}(1 - e^{-\tau_{tot}}) \quad (34)$$

where T_{ex} is the excitation temperature, which is related to the ratio of energy level populations through the Boltzmann equation. In particular, the population ratio $n_u/n_l = (g_u/g_l) \exp(-\Delta E_{u,l}/kT_{ex})$, where g_u and g_l are the statistical weights ($2F=1$ for the 21 cm HI line). We can calculate the change in brightness temperature by subtracting $T_b(0)$ from both sides of equation (34).

$$\Delta T_b = T_b - T_b(0) = \{T_{ex} - T_b(0)\}(1 - e^{-\tau_{tot}}) \quad (35)$$

We can see from equation (35) that if the excitation temperature, T_{ex} , is less than $T_b(0)$, then ΔT_b is negative. If ΔT_b is negative then radiation has been absorbed.

2.5. Aperture Synthesis Observations

Results presented below for the W3 star forming region in our Galaxy were obtained with the Very Large Array (VLA), operated by the National Radio Astronomy Observatory near Socorro, NM. This radio telescope system consists of 27 radio telescopes, each 25 m in diameter. The VLA operates on the principle of interferometry where the spatial resolution of the system (in angular units on the sky) is not determined by the size of an individual radio telescope but by the separations of individual *pairs* of radio telescopes. The 27 antennas operate simultaneously as 351 (i.e. $n*(n-1)/2$, where n is the number of antennas) interferometer pairs. Each pair measures a Fourier component of the brightness distribution (i.e. the image) of the desired radio source in the sky. Antenna pairs with greater separations measure higher spatial frequencies, providing information about smaller angular scale features in the image. Likewise, antenna pairs with smaller separations provide information about larger angular scale features of the image. Moreover, the effective separation of a given pair of antennas (the baseline) changes with time during an observation as the radio source moves across the sky owing to Earth rotation. The reason for this change is that the effective baseline is not the true separation of the two antennas on the ground but the projected separation as viewed from the radio source. As a result, a multi-hour observation of a given radio source with all VLA antennas yields a large number of individual measurements of Fourier components

of the image of the source. After the observations are complete, the data analysis process undertakes a Fourier transformation of these data into the image of the source. In practice, this process yields not a single image but a series of images (typically 128 or 256) of the source at narrow, adjacent frequency intervals. From this series of images (or image cube), a spectrum can be extracted at any pixel in the data. Note that the VLA antennas are periodically (several times per year) moved into different configurations. In the D configuration, the antennas are relatively close together, so baselines are short, and the array is sensitive to larger angular scale features in the source image. The C, B and A configurations have the antennas progressively more separated. Baselines are progressively longer, and the array is sensitive to smaller angular scale features, that is, the spatial resolution becomes higher. Often, and this is the case for the W3 observations described below, VLA data from different configurations, gathered at different times, are combined. In such a combined data set, the image of the source reveals both large and small angular scale features. Such an image has higher fidelity to the true source image than an image made from data from a single VLA configuration. The technique of combining information from a large number of radio telescopes interferometrically is known as *aperture synthesis*. In effect, this technique provides some of the information that would be provided by a single radio telescope whose diameter equals the longest baseline of the array. In that sense, an aperture is synthesized by the VLA radio telescopes operating together, an aperture much larger than could be constructed as a single radio telescope.

2.6. Other Important Quantities

There are many other important physical quantities in astrophysics, far too many to list in this document. However, there are some more quantities that need to be defined. These are oscillator strength and column density. Oscillator strength is a dimensionless number which describes the probability of a particular quantum mechanical transition. Higher oscillator strengths indicate more probable transitions. The primary purpose for mentioning oscillator strength in this document is because it is used in the calculation of one of the other important quantities, column density. Column density is simply the number of particles of a particular type (e.g. Fe^+) per unit area along an imaginary cylinder. Typically the area unit is cm^2 so that the units of column density are cm^{-2} . The relationship between oscillator strength and column density is given in chapter 4 (equation 37).

3. Chapter Three: W3 Region

3.1. Overview of W3

W3 is an H^+ region and molecular cloud complex located about 2 kpc away from Earth in the Perseus Arm of the Galaxy. W3 lies close to other star forming regions in the Perseus Arm, most notably those associated with H^+ regions W4 and W5. Further indications of recent star formation in the vicinity include the Cas OB6 stellar association and the supernova remnant (SNR) HB3. The hot, luminous stars of the Cas OB6 association have very short lifetimes (a few to a few 10s of millions of years) before destruction via supernova explosions. Therefore, the presence of these stars today, as well as the presence of a SNR, indicates that star formation has occurred recently in this region. Also, H^+ regions themselves are indicators of recent star formation since they are formed by the same hot and short-lived stars; and the H^+ regions, owing to their high temperatures, expand and dissipate on relatively short timescales. W3, W4, and W5 form a chain of H^+ regions for which there is little overlap along the line of sight. As reported in Dickel (1980) and Thronson (1985), W4 was probably the first of these three H^+ regions to form. The expansion of W4 is likely responsible for the most recent OB star formation which has occurred at the eastern edge of W3, called the high density layer (Lada 1978). The interaction between W4 and W3 may be an example of hierarchical triggered star formation (Oey et al 2005). The SNR HB3 is a shell type remnant which lies to the west of the W3 complex. Due to its proximity to W3, HB 3 is also believed to have played a role in the collapse of the western side of W3. W3 is the youngest of all of these three regions containing several masers (Normandeau 1997).

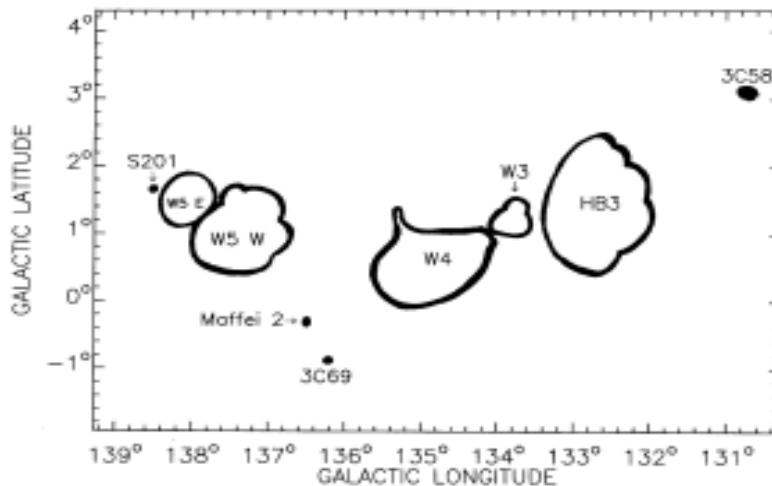


Figure 3.1: This is a figure from Normandeau (1997) which shows the relative positions of W3, W4, W5, and HB3 based on continuum emission.

H^+ regions like W3 are the source of radiation over a wide range of wavelengths. For example, they often appear red in optical images owing to the radiation of H atoms that have temporarily formed by recombination of free electrons and protons. During such recombination events, the newly-formed atoms cascade down from upper principal quantum numbers to lower numbers, emitting photons along the way. Radiation from the transition $n = 3$ to 2 corresponds to a wavelength of 656 nm, appearing red to the eye.

Another type of radiation from H^+ regions occurs in the radio region of the spectrum. Often referred to as “free-free” emission, this radiation arises as an electron is accelerated by a nearby proton. The accelerated charge emits a photon whose exact energy depends upon the proximity of the encounter. The result of an ensemble of such electron-proton encounters in an H^+ region is radio emission spread over a very broad range of wavelengths. Such radiation, emitted by the free-free process, is often termed radio continuum emission.

W3 is a region of active star formation that is divided into 3 main H^+ regions: W3 Main, W3 North, and W3 OH. W3 Main, composed of W3 East and W3 West, contains several H^+ regions driven by a collection of embedded O and B stars. It is the most active region of star formation in the W3 GMC, containing more than 10 OB stars (Tieftrunk 1997, 1998). Normandeau (1997) measured the 1420 MHz radio continuum flux density of W3 Main to be 76.6 Jy. In the W3 East region there are two O stars at the eastern edge, an O8 and an O7. The O8 star is considered by Garmany (1992) to be part of the Cas OB6 association. The position of these stars, both on the eastern edge of the region, means that they cannot be solely responsible for the ionization of this region. W3 East also contains four bright infrared stars. Within 1 arc minute of the center of W3 West there are 5 bright infrared stars as well as 3 masers. W3 West can be subdivided into 10 or more compact H^+ regions. W3 A and B are two prominent H^+ regions in the northeast of W3 West. Between them lies the infrared source, IRS5. W3 C, D, and H occupy the northwest corner of W3 West. The two southern H^+ regions of W3 West are known as W3 K and W3 J.

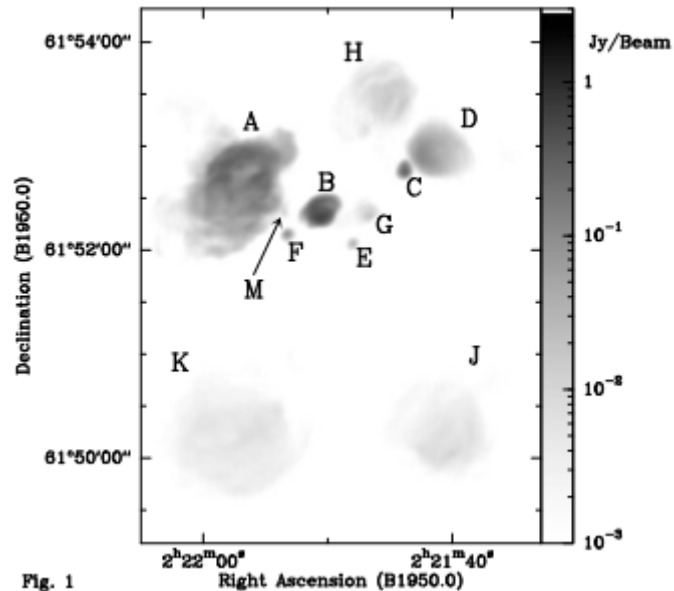


Figure 3.2: This is a continuum map of W3 from Tieftrunk (1997) with the H^+ regions labeled.

Tieftrunk (1995) mapped a $3' \times 2'$ area of the W3 molecular cloud using the $J=2-1$ transition of ^{18}CO and the $J=3-2$ and $J=5-4$ transitions of C^{34}S . Radio spectral line emission from these molecules is considered a tracer of H_2 in the ISM. Moreover, the mass of H_2 material can be inferred from this molecular line emission given assumed ratios of tracer molecules to H_2 . Tieftrunk (1995) found that the total molecular mass of

W3 ranges from 2500 – 3000 solar masses and the molecular cloud associated with IRS 5 is between 800 and 1200 solar masses with an average H_2 column density of $2.1 \times 10^{23} \text{ cm}^{-2}$. Tieftrunk (1995, 1997) noticed that the molecular gas and the ionized gas do not appear in the same locations. This supports the idea that the ionized regions have pushed the molecular gas away. Figure 3.3 (from Tieftrunk et al 1995) shows both the 21 cm continuum and the column density of $C^{18}O$. In this case, $C^{18}O$ is being used as a tracer of H_2 . Assuming that the ratio of $C^{18}O$ to H_2 is the same everywhere in the W3 region, we can then infer that the contour lines in Figure 3.3 represent the amount of molecular hydrogen gas. Figure 3.3 shows that the bulk of the H_2 gas is around IRS 5 (shown by the number “5”) and IRS 4 (just below “D” in Figure 3.3). These molecular clouds are referred to as the IRS 5 and IRS 4 molecular clouds respectively.

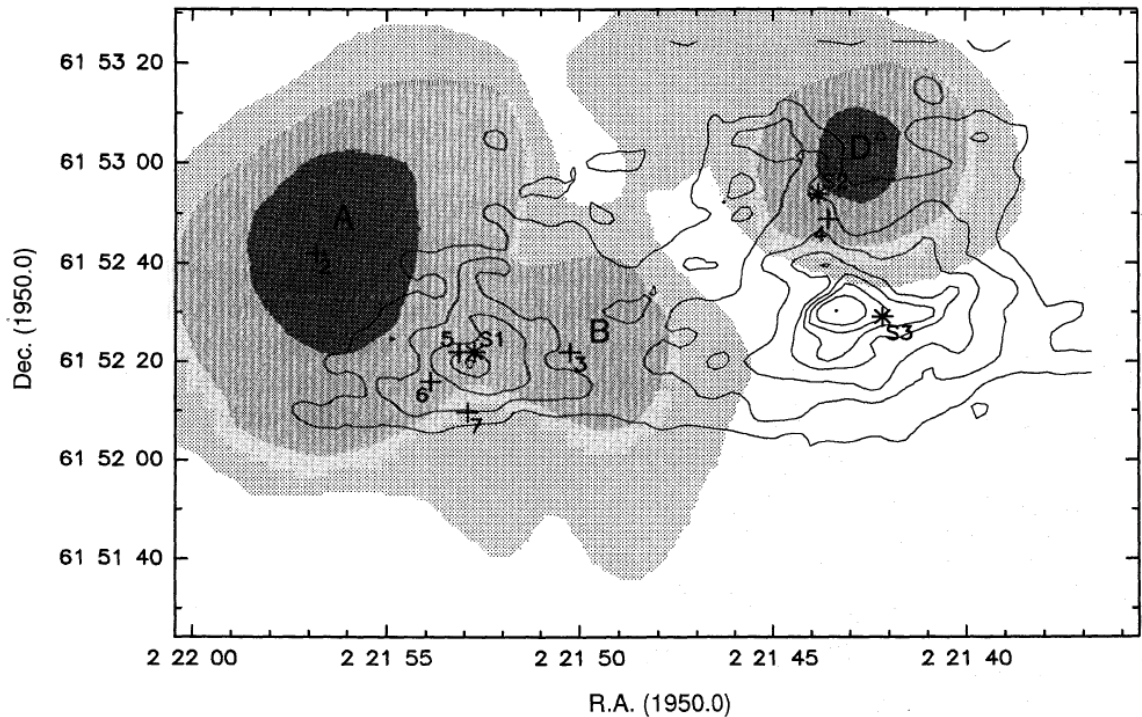


Figure 3.3: This is a map presented in Tieftrunk et al (1995). The grayscale represents the 21 cm continuum while the contours show the column density of the tracer $C^{18}O$.

W3 Main, W3 OH, and W3 North show very different low mass stellar populations. W3 Main is a large nearly spherical cluster. It does not show evidence that it has been recently triggered; it is not patchy and elongated. It was then likely formed in an earlier episode. Ojha (2004) detected a large number of pre-main sequence stars arranged from northwest toward southeast in the W3 Main region. The pre-main sequence population of W3 Main resembles those of Orion M17, and Rosetta Nebulae. However, W3 Main OB stars are very recently formed and are still surrounded by H^+ regions embedded within dense clumpy molecular cores. This is different than the other regions mentioned above as their H^+ regions have merged into a large blister and have dispersed their natal clouds. The OB stars that are exciting the H^+ regions of W3 Main recently formed and are considerably younger than the hundreds of x-ray emitting pre-main sequence stars that are spread over several parsecs (Feigleson 2008).

The two other regions of W3 are W3 OH and W3 North. W3 OH contains an ultra compact H⁺ region and hot molecular core, several OH and methanol masers and deeply embedded young O stars. Hachisuka (2006) measured the distance to W3 OH using water maser annual parallax to be 1.95 kpc. Its stellar population is arranged in an elongated group of sparse stellar clumps. W3(OH) structures are consistent with collect and collapse triggering process caused by shocks from the older IC 1795 cluster. The W3 North region is ionized by a single O8 star according to Ogura 1976. Within 1 arc minute of the center of W3 North there are four bright infrared stars. Normandeau (1997) measured the 1420 MHz integrated flux density to be 26.4 Jy.

3.2. Previous Magnetic Field Studies

Troland (1989) detected line of sight magnetic field strengths of 100 μG near W3. They measured the 1420 MHz H I line using the D array configuration of the VLA. Their magnetic field map shows that field reverses direction between W3 A and W3 B. Troland (1989) proposed an hourglass model to explain the field reversal. Roberts et al (1993) estimated line of sight magnetic field values for W3 using 5 hours of C array data and 1 hour of D array data. They observed the Zeeman Effect in two different velocity components, -38 and -46 km s^{-1} . For the -38 km s^{-1} component, line of sight magnetic fields stronger than $-100 \mu\text{G}$ for W3 A and $+200 \mu\text{G}$ for W3 B were found. They confirmed the field reversal observed by Troland and supported an hour-glass model of the magnetic field toward W3 A and W3 B. In the -46 km s^{-1} component, they found a weak positive line of sight magnetic field. Roberts et al (1993) also used statistical summing (see section 3.3) to estimate the line of sight magnetic fields in several regions to the south of W3 A and B referred to as NGC 896. In the -38 km s^{-1} component they found field strengths ranging from -38 to $+43 \mu\text{G}$. They found a range of -40 to $+19 \mu\text{G}$ for the -46 km s^{-1} component.

Roberts et al (1997) used the Berkley-Illinois-Maryland Association (BIMA) array to observe ^{13}CO and C^{18}O and estimate the masses of six H₂ clumps associated with IRS 4 and IRS 5. IRS 4 lies approximately $14''$ west of W3 A while IRS 5 lies directly between W3 A and W3 B. To estimate the H₂ masses, Roberts et al (1997) first measured the column density of ^{13}CO and then used the ^{13}CO to H₂ ratio (2×10^{-6} from Dickman 1978) to find the column density of H₂. At IRS 5, they estimate $N(\text{H})$ to be $4.6 \times 10^{23} \text{ cm}^{-2}$. They used $N(\text{H})$ and the total magnetic field strength of 1 mG from Roberts et al (1993) to find the magnetic field-to-column density ratio. The magnetic field-to-column density ratio is proportional to the critical flux-to-mass ratio determined by Mouschovias & Spitzer (1976). Mouschovias & Spitzer found that $|B_{\text{crit}}|/N(\text{H}) = 1.6 \times 10^{-21} \mu\text{G cm}^{-2}$ is the minimum value for which a magnetic field can support a cloud against gravitational collapse. Roberts et al (1997) found $|B|/N(\text{H}) = 2 \times 10^{-21} \mu\text{G cm}^{-2}$ for the region near IRS 5 (W3 A and B). They concluded that the magnetic field in this region is capable of supporting the clouds against gravitational collapse.

The goal of this project was to extend significantly the study of Roberts et al (1993). Compared to the data used by Roberts et al, we have 5 times the amount of D array data,

as well as 20 hours of AB array data. The D array data was added to resolve large scale structures south of the W3 A and B and the AB array data was added to increase the spatial resolution. This project should provide the most accurate line of sight magnetic field measurement of this region and tell us if the hourglass model of the field still stands.

3.3. Observations and Data Reduction

Table 3.1 lists the observational parameters used in these measurements. The 21cm H I absorption observations were carried out using the Very Large Array (VLA). Right and left circular polarizations were observed simultaneously and the electronics for each sense of polarization were alternated every 10 minutes to mitigate instrumental effects. The Astronomical Image Processing System (AIPS) was used to edit, calibrate, Fourier transform, and deconvolve the H I data. Bandpass calibration, of only Stokes I, was completed using the flux calibrator 0134+319. Gain correction, cleaning of V, and the magnetic field estimates were carried out using MIRIAD. We determined the line of sight magnetic field in by fitting the numerical derivative of the Stokes I spectrum to the Stokes V since Stokes V and Stokes I are related by

$$V = 2.8B_{los} \frac{dI}{d\nu}. \quad (36)$$

For areas where there was significant evidence for the Zeeman Effect in the Stokes V spectrum, for W3 A and W3 B, we fit derivative on a pixel by pixel basis using the MIRIAD task Zeemap. Figure 3.4 shows the Stokes I profile and the Stokes V profile with the fitted derivative of I for a pixel of high magnetic field. In regions, like south of the W3 core, where the Zeeman Effect is less evident, we chose to use the task Zeestat. Zeestat estimates the magnetic field using the statistical summing method. Statistical summing is a process used to approximate the magnetic field in regions of low surface brightness. To approximate the magnetic field for a region, all of the pixels for that region are selected. The Stokes I spectra for the selected pixels are strung together end to end. The same process occurs for the Stokes V spectra. Now the numerical derivatives of all of the selected Stokes I spectra are fit to all of the Stokes V spectra. This process leads to a single “average” magnetic field for the selected region. Unfortunately, the errors reported by Zeestat are unrealistically low so we also used a task called Zeesim. Zeesim produces a “fiddle factor” to correct the error output of Zeestat through a fitting simulation.

Table 3.1: Observing Parameters for W3

Observing Dates	1990 December 1991 January, March
-----------------	-----------------------------------

	1993 October
	1994 June
Total Observing Time	20.9 hours in VLA - AB Configuration
	5.1 hours in VLA - C Configuration
	5.0 hours in VLA - D Configuration
Primary Beam Width HPBW	30'
Phase and Pointing Centers	$\alpha_{2000}=2h25m37s$, $\delta_{2000}=62deg3m32s$
Synthesized Beam HPBW	5" x 5"
Spectrometer	128 frequency channels per polarization
	Total Bandwidth 195.3 kHz (40 km s^{-1})
	$V_{\text{LSR}} = -63 \text{ to } -23 \text{ km s}^{-1}$
	Channel separation 1.526 kHz (0.32 km s^{-1})
Frequency resolution 1.526 kHz (0.32 km s^{-1})	
Conversion to Linear Scales	1' = 0.6 pc

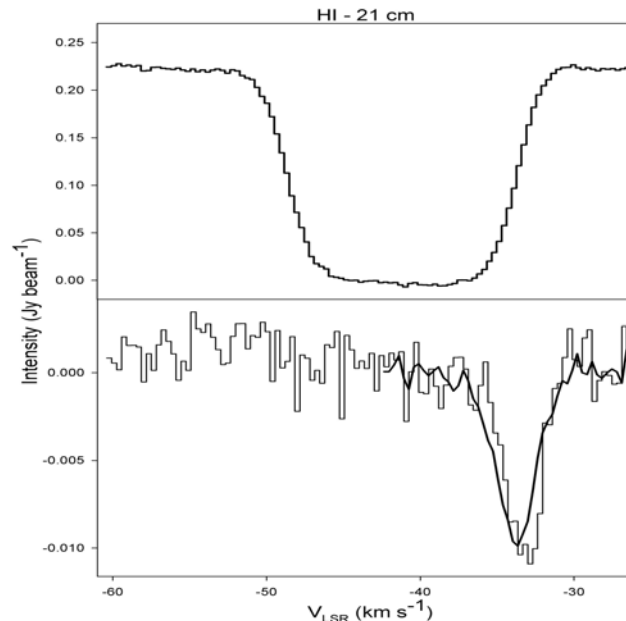


Figure 3.4: The top portion show the Stokes I profile of the 21 cm absorption line. The Stokes V profile (histogram plot) and the scaled derivative of Stokes I (dark line).

3.4. Results

Figure 3.5 is a map of the 21 cm continuum. All of the H^+ regions that are labeled in Figure 3.2 are visible in this image. The two most important of these regions, at least for magnetic fields, are W3 A and W3 B. Figure 3.6 is the same continuum map as Figure 3.5, but here it is zoomed in on W3 A and B. Both Figure 3.4 and Figure 3.5 show contour lines representing the continuum levels. The contour lines are at 10%, 25%, 50%, and 75% of the maximum flux which is approximately 0.26 Jy/beam. The semi-spherical symmetry of these H^+ regions is likely not coincidental. As mentioned in chapter 1, H^+ regions are thought to form when bright O and B type stars are formed inside a molecular

cloud. The dissociation and ionization of the molecular gas surrounding the star should be spherically symmetric if the gas around the star is homogenous.

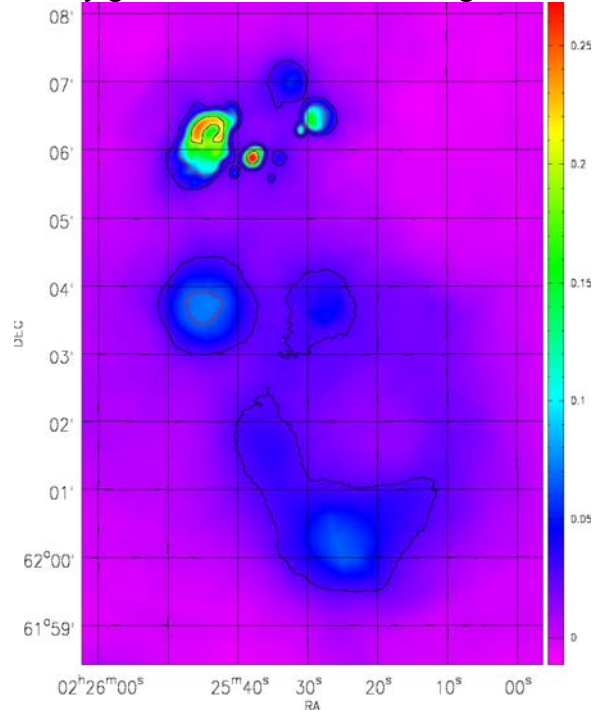


Figure 3.5: Continuum Map of W3 and NGC 896. Contour levels are 10%, 25%, 50%, and 75% of the peak flux (about 0.26 Jy/beam)

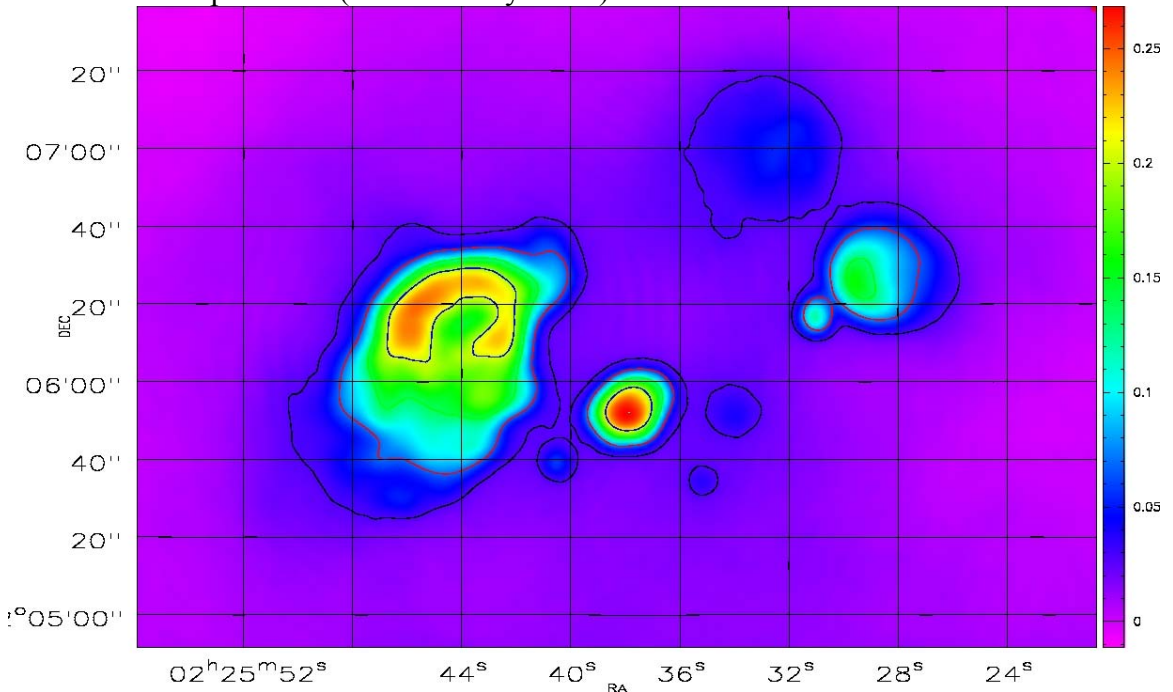


Figure 3.6: This is a more detailed view of the W3 portion of the continuum map. Contour levels are 10%, 25%, 50%, and 75% of the peak flux (about 0.26 Jy/beam)

Using the pixel by pixel method described (Zeemap) above we find significant magnetic fields for the -38 km s^{-1} component, see Figure 3.7, in both the W3 A and W3 B

regions. Magnetic fields are deemed significant if the field strength is greater than three times the 1σ error. For W3 A, we find significant magnetic field detections ranging from $-100 \mu\text{G}$ in the southeast to $-500 \mu\text{G}$ in the northwest. We find the magnetic field in W3 B to range from 300 to $700 \mu\text{G}$. The field is consistent in the central and southern portions of W3 B but it peaks sharply at the northern side. The magnetic field detections in the -46 km s^{-1} component, Figure 3.8, are sparse compared to the -38 km s^{-1} . Most of the detections in the -46 km s^{-1} component are in W3 A and on the order of $100 \mu\text{G}$. In the southern portion of our field of view, NGC 896, we saw no evidence of the Zeeman Effect in the Stokes V profile. Therefore, we used statistical summing to extract a magnetic field value. We performed the summing over the 3 regions specified in Roberts et al 1993 but we found no significant magnetic field detections.

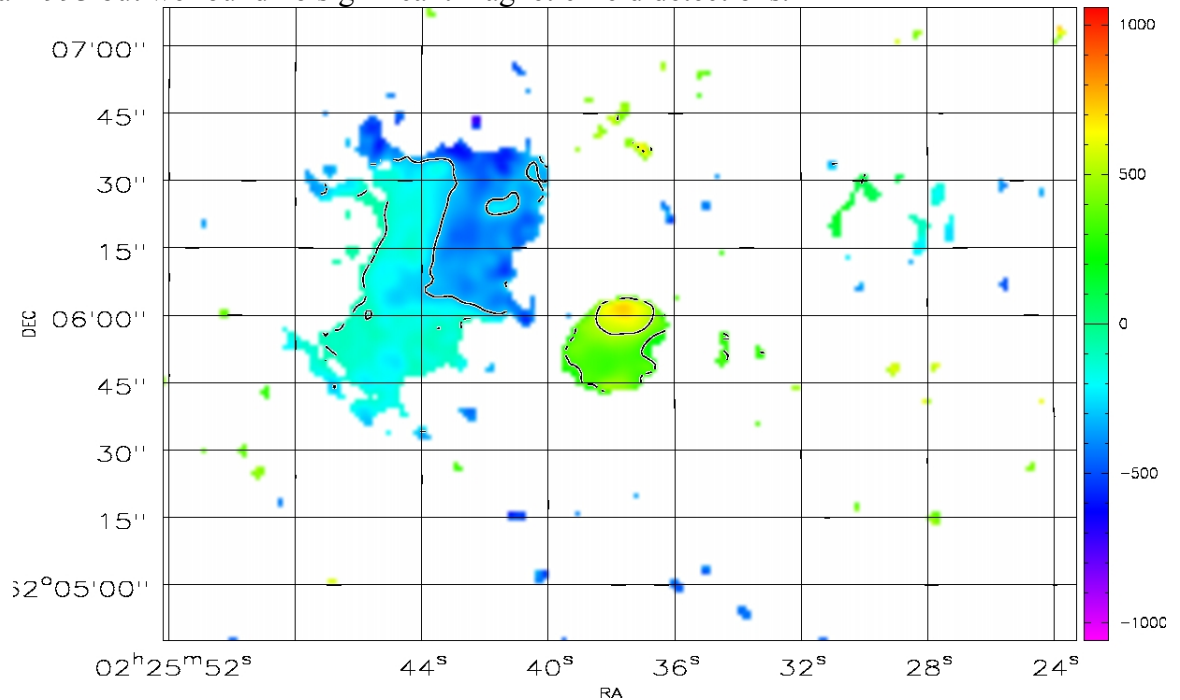


Figure 3.7: This is the magnetic field map of the -38 km s^{-1} component. The image has been masked to only display pixels where the field is more than 3 times the error. The contour levels are -300 , -100 , 100 , 300 , and 500 microgauss.

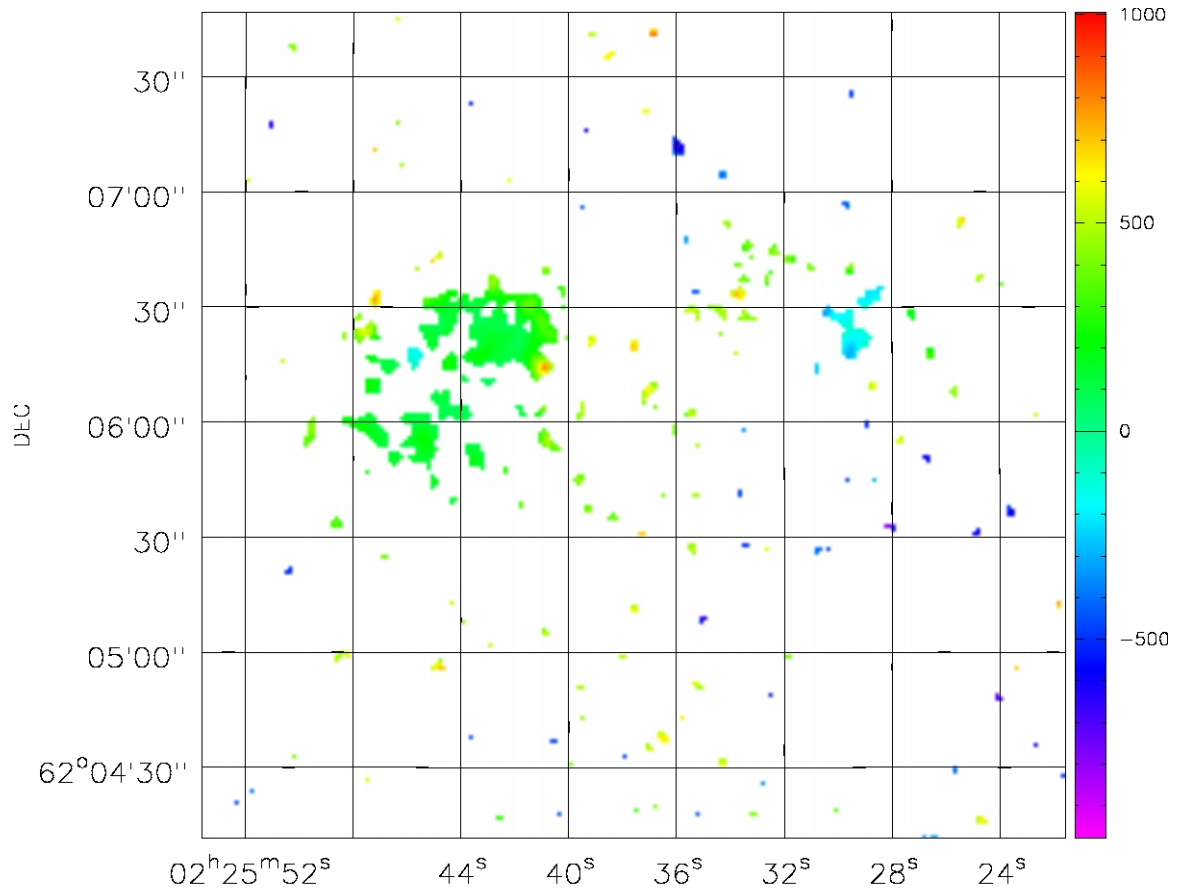


Figure 3.8: This is the magnetic field map of the -46 km s^{-1} component. The image has been masked to only display pixels where the field is more than 3 times the error. There are no contours since there are few regions of consistent detection.

3.5. Discussion

In order to directly compare to Roberts et al (1993), we used statistical summing in the 5 regions that he did. The values are listed in Table 3.2.

Table 3.2: Magnetic Field Results vs. Roberts et al

Component	$B_{\text{los}}(-38 \text{ km s}^{-1}) (\mu\text{G})$	Roberts $B_{\text{los}}(-38 \text{ km s}^{-1}) (\mu\text{G})$	$B_{\text{los}}(-46 \text{ km s}^{-1}) (\mu\text{G})$	Roberts $B_{\text{los}}(-46 \text{ km s}^{-1}) (\mu\text{G})$
W3 A	-166 ± 12	-47 ± 3	45 ± 13	18 ± 3
W3 B	388 ± 26	103 ± 7	46 ± 24	15 ± 4
NGC 896(1)	-27 ± 38	43 ± 7	31 ± 44	18 ± 6
NGC 896(2)	-33 ± 20	-38 ± 5	2 ± 30	19 ± 5
NGC 896(3)	-33 ± 23	-38 ± 5	-8 ± 32	-40 ± 7

For W3 A and W3 B, our magnetic field values are higher than those of Roberts et al (1993) but they are consistent in sign. Our higher magnetic field values are likely due to higher spatial resolution. We find no significant magnetic field detections for any of the sampled regions of NGC 896. However, our values including errors overlap with the results of Roberts et al (1993) in every case except for the -38 km s^{-1} component in NGC 896(1). It should be noted that the errors in Roberts et al (1993) are considerably lower than ours. One possible explanation for the very low errors is that Roberts et al (1993) did not use the MIRIAD task Zeesim. Roberts et al (1993) does not explicitly state whether Zeesim was or was not used. If Zeesim was not used, then the Roberts et al errors should be higher which would reduce the number of significant detections.

3.6. Model

The hourglass model was proposed by Troland (1989) and confirmed by Roberts et al (1993) to explain the magnetic field reversal between W3 A and W3 B. Figure 3.9 is a simple diagram that illustrates the hourglass model. Imagine a cloud with a uniform magnetic field passing through it. As the cloud contracts, the magnetic field lines will contract as well as long as the gas is flux frozen to the field. The magnetic field lines are now in the shape of an hourglass, narrower in the middle and wider at the ends. This has the effect of increasing the magnetic field strength inside the cloud. It also means that an appropriately placed observer, at the bottom of the figure, would see a field reversal in the line of sight component of the magnetic field. On the right side of the cloud, the observer would measure the magnetic to be positive. This means that the line of sight component of the field is pointing away from the observer. The observer would measure the opposite on the left side of the cloud. This is basically what we see in W3 A and B. The field is positive near W3 B (to the west of the IRS 5 molecular cloud) and it is negative near W3 A. We can then infer that W3 A and W3 B were likely part of the IRS 5 GMC in the recent past. Star formation near the centers of what are now W3 A and W3 B dissociated and then ionized the molecular gas via ultraviolet photons. The continued contraction of the IRS 5 GMC and the expansion of the H^+ regions probably created the hourglass shape in the magnetic field lines. While the physical situation is most certainly more complex, this model, though simple, is a good approximation of what is happening in W3.

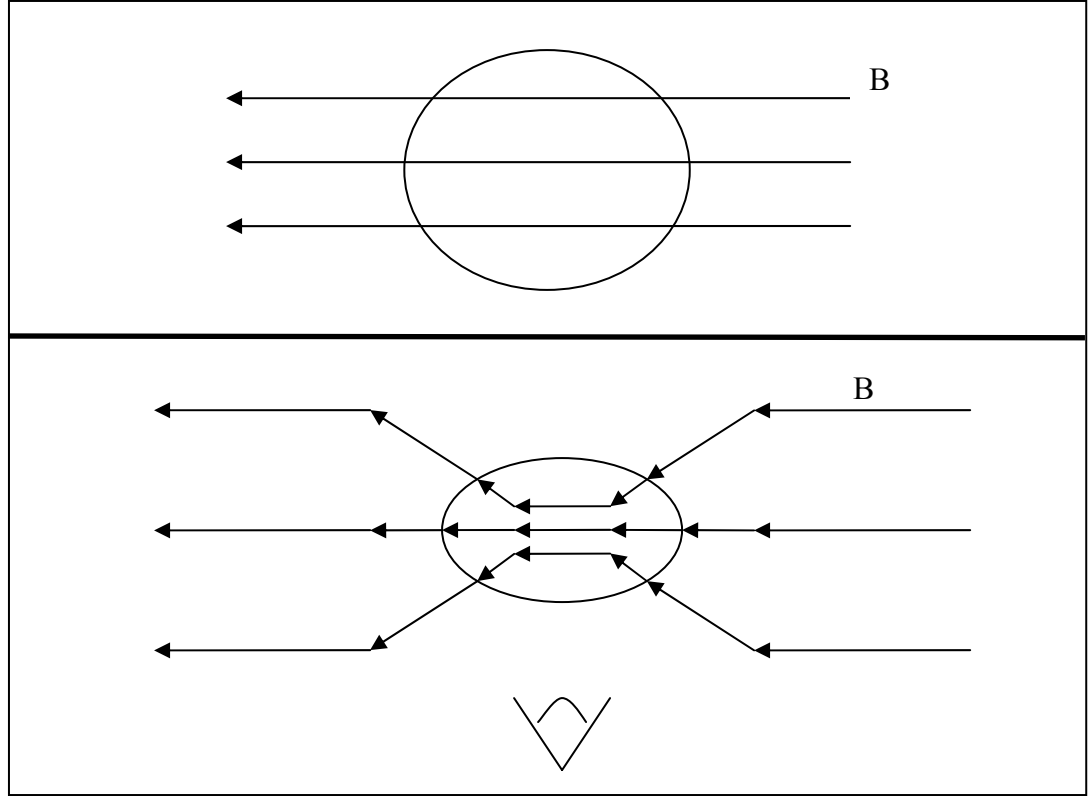


Figure 3.9: The top image represents a uniform magnetic field passing through a GMC. The bottom image shows what happens to the magnetic field if the GMC contracts. The observer at the bottom would see a line of sight field reversal from one side of the contracted cloud to the other. Note that actual magnetic field lines would be smooth.

3.7. Energetics

From our measurements of the magnetic field, along with values from Tiefrunk (1995), we can estimate the gravitational, total internal, and the magnetic energies of the region using equations (11), (13), and (14). To use equation (11) we need to know the mass and radius of the cloud. We estimate the radius of the cloud (assuming it to be spherical) by measuring the angular size of the cloud using Figure 3.3. We find the molecular cloud to have an angular size of approximately 0.43 arc minutes. When combined with the distance to W3, 2 kpc, we are able to approximate the radius of the cloud. The mass of the cloud comes from multiplying the proton column density, which was taken to be $4.2 \times 10^{23} \text{ cm}^{-2}$ from Tiefrunk et al. (1995), by the area of the cloud and by the mass of a proton. That mass is then divided by the mass of the Sun to give us a total mass for the cloud of 926 solar masses. Using equation (11), we find the total gravitational potential energy for W3 to be 2.1×10^{47} ergs. To calculate the kinetic energy we used the FWHM velocity dispersion of 3.50 km s^{-1} given in Tiefrunk et al. (1995). The kinetic energy is 6.1×10^{46} ergs. For the magnetic energy, equation (14), we need the magnetic field and the radius. Supplying our magnetic field and using the radius calculated above, we find the magnetic energy to be 2.2×10^{46} ergs. We compared the magnetic energy to the gravitational energy with the mass to flux ratio, equation (18). We

found $\lambda = 3.0$, which means that W3 is magnetically supercritical and cannot be supported by the magnetic field alone. By putting the energy values into equation (16), we calculated the virial energy ratio to be 0.7. The magnetic energy is approximately 10% of the gravitational energy for W3 while the thermal energy is about 58%. However, the errors associated with these calculations are significant. Considering the errors we conclude that W3 is or is nearly in virial equilibrium. This is consistent with the results of Roberts et al (1997).

3.8. W3 Conclusions

The primary goal of this project was to expand on the work of Roberts et al (1993) by adding higher resolution and more sensitive data. By measuring the 21 cm absorption line toward W3 in both LCP and RCP simultaneously, we were able to measure the line of sight magnetic field for different positions in this region. Near the H^+ regions of W3 A and W3 B our line of sight magnetic fields were consistent in sign but higher than those of Roberts et al. The higher field strengths, relative to those of Roberts et al. are very likely the result of higher spatial resolution in the more recent data. Our beam size is $5'' \times 5''$ while the beam size of Roberts et al (1993) is $25'' \times 25''$. The higher spatial resolution can resolve smaller regions in the source having locally high field strengths. We failed to detect any significant field in the southern regions unlike Roberts et al. (1993) but we believe this discrepancy is due to a bug in the error calculation of the MIRIAD task Zeestat. By looking at how the magnetic field changed with position it was possible to create a simple model for the magnetic field morphology. We found that the line of sight field reversed direction from W3 B to W3 A. This led us to conclude that the magnetic field in the region has an hourglass shape which confirms the results of Roberts et al (1993) and Troland (1989). With our measurements of the magnetic fields we were able to calculate the various energies associated with W3. We found that W3 is magnetically supercritical and lacks sufficient support from both the magnetic field and from thermal motions to hold up against gravity.

4. Chapter Four: Orion's Veil

4.1. Overview of the Orion's Veil Region

Orion, “The Hunter”, is one of the most recognizable constellations in the night sky. Located between Taurus, Canis Major, and Gemini, Orion is easily identified by the 3 stars that make up Orion's Belt. Orion's right shoulder (assuming he is facing the observer) is represented by Betelgeuse. Betelgeuse is a red supergiant and the second brightest star in the constellation of Orion. The brightest star in Orion is Rigel. Rigel is a blue supergiant that is about 17 times more massive than the Sun. At the tip of the sword hanging from Orion's Belt are several stars, which make up the Trapezium, and the Orion Nebula (M42). The Trapezium is a tight cluster of stars within M42 which provide much of its illumination. The most recognizable feature of the Trapezium is the four stars which form a box shape. These stars are named Θ^1 A, Θ^1 B, Θ^1 C, and Θ^1 D Orionis in order of increasing right ascension. Θ^1 C is the brightest of the four.

The Orion Nebula, M42, is the closest region of massive star formation to the Earth. It is no surprise then that it is also one of the most studied regions in the universe. Most of the radiation from M42 comes from a region that is a few arcminutes across called the Huygens Region (Figure 4.1). M42 is a concave H^+ region that formed out of the Orion Molecular Cloud (OMC-1) that happens to face the Sun.

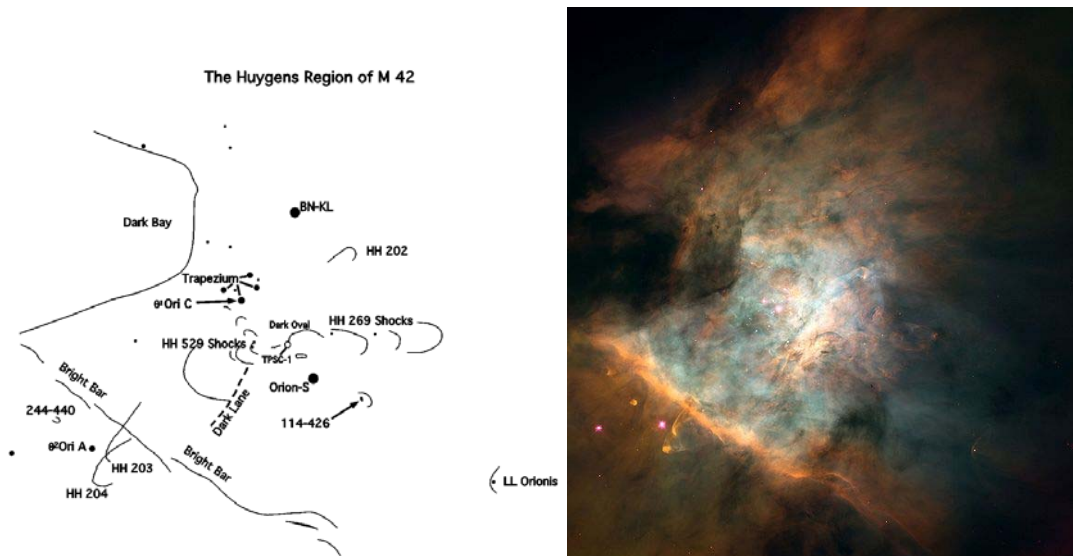


Figure 4.1: To the left is a map showing the constituents of the Huygens Region of M42 and their relative locations from O'Dell (2001). On the right is an image taken by the HST (O'Dell 2000).

One prominent feature of M42 is the Bright Bar. The Bright Bar is part of the main ionization front (MIF). This is where stellar radiation from the Trapezium is dissociating and ionizing the molecular gas of OMC-1. It appears as a thin line because we are viewing it edge on. Another feature of M42 is called the Dark Bay. The Dark Bay is a region where much of the optical radiation is absorbed or scattered; It has a high visual extinction, A_V . The dust and gas that compose the Dark Bay absorb the visible

light that tries to pass through it. The Dark Bay is not the only part of the Huygens Region of M42 that suffers from extinction. The entire nebula is covered by a veil of dark material called Orion's Veil.

Orion's Veil is a region of predominately neutral hydrogen that exists between the Earth and the trapezium stars. Orion's Veil is between 1 and 3 parsecs from the Trapezium and 500 parsecs from Earth. Figure 4.2 is a simple diagram of the Veil. The solid gray color represents molecular hydrogen, while the checker pattern is atomic hydrogen. The small-dotted pattern shows ionized hydrogen. Figure 4.2 shows no molecular hydrogen in Orion's Veil. The reason for this is because ultraviolet (UV) photons from the Trapezium stars prevent molecular hydrogen from forming. The intense UV flux is also why there is a thin strip of ionized hydrogen on the side of the veil facing the Trapezium. Figure 4.2 also shows Orion's Veil to be in two separate blocks. This represents the two different velocity components that were observed in the 21 cm H I absorption profile by Abel (2004). The heliocentric velocities (with respect to the Sun) of these two components are 19.4 and 23.4 km s^{-1} .

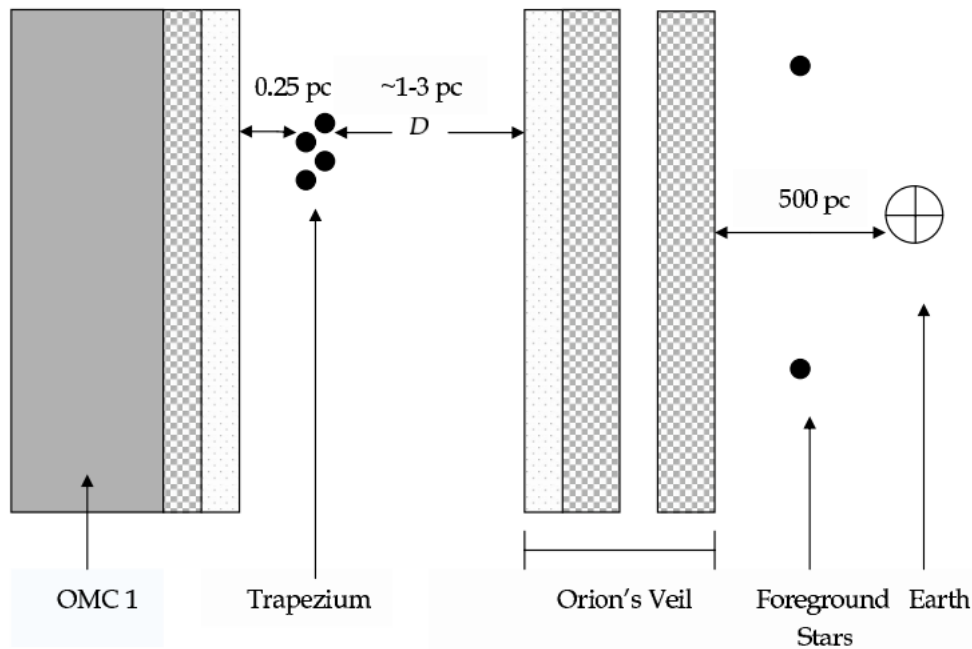


Figure 4.2: This is a diagram from Abel et al. (2004) showing the position of Orion's Veil relative to the trapezium stars as well as the phase of hydrogen at a given location. The solid gray color represents molecular hydrogen, the checker pattern is atomic hydrogen, and the small-dotted pattern shows ionized hydrogen.

In addition to the hydrogen gas, Orion's Veil contains gas from heavier elements and dust grains. The dust is composed of the heavier elements in the solid phase. It is unknown exactly how the first grains form. However once a solid grain is present, it is easier for other heavy elements to condense onto the grains. The rate at which atoms condense onto the grains is likely proportional to the density of the region. Grains can also be destroyed if enough energy is present for them to sublimate. What physical processes could be responsible for grain destruction?

4.2. Previous Magnetic Field Studies

There have been several measurements of the magnetic field in Orion's Veil. Troland et. Al. (1989) used the VLA to map the Zeeman effect in the 21 cm H I absorption lines in Orion's Veil along the line of sight toward Orion A. They were able to determine the magnetic field for each of the velocity components in the veil. They found that the line-of-sight magnetic field is approximately 50 μG and pointed toward the Earth. Troland et. Al. (1989) found that the magnetic energy is the dominant form of energy in this region over thermal, macroscopic motions, and even gravitational.

4.3. Introduction to Measuring the Depletion of Iron

Ultraviolet absorption lines provide a relatively straightforward method of measuring interstellar abundances along the lines-of-sight to early type stars. As long as the lines are not too optically thick, and they arise from species in their principal ionization states, they yield direct measures of column density, subject primarily to uncertainties in oscillator strengths. In this project we report upon an analysis of archival high-spectral resolution Hubble Space Telescope (HST) Space Telescope Imaging Spectrograph (STIS) Fe absorption lines along the line of sight to star Θ^1 B Orionis (HD 37021). These data provide information about depletions and other physical characteristics of the interstellar gas along this line-of-sight.

Iron must make up a significant portion of the mass of interstellar grains even though there is no direct spectroscopic evidence for its presence in the solid state. This conclusion is based upon the fact that Fe is a cosmically abundant element, yet it is heavily depleted in the interstellar medium. If most of the Fe in the ISM is depleted onto grains, then grain destruction mechanisms will return a fraction of the Fe to the gaseous state where its increased abundance can be measured. Therefore, studies of the gas phase Fe abundance can reveal information about grain destruction processes.

Grain destruction is believed to occur via a variety of processes, the most important of which may be high speed ($\approx 100 \text{ km s}^{-1}$) shock waves associated with SNR. (See review by Jenkins 2004.) However, it is also possible that grains are partially destroyed in the harsh environments of H^+ regions via sputtering, evaporation or optical erosion. (See discussion by Osterbrock 1989 and Rodriguez 2002.) In particular, Rogriguez (2002) argues that grain destruction occurs in H^+ regions, based upon a correlation between Fe abundance in the ionized gas and the degree of ionization.

Orion is an excellent place to search for evidence of grain destruction in ionized gas. The Fe abundance in the H^+ region has been measured by several investigators (§ 4.6.1). Moreover, there is the neutral Veil of material lying 1 to 3 pc in front of the H^+ region (Abel et al. 2004, 2006 and references therein). Since the Orion Veil is so close to the H^+ region, it was almost certainly formed from the same interstellar cloud. Therefore, total abundances of the elements (gas and grains combined) are very likely to be the same in the neutral and ionized regions. Also, the principal Veil velocities are comparable to those of the Orion H^+ region and the background molecular cloud. Therefore strong shocks are unlikely to have affected the Veil and therefore are unlikely to have destroyed grains. If grain destruction has occurred in the Orion H^+ region, then this process should result in a measurably higher Fe/H in the ionized gas compared to the neutral Veil. A principal goal of work reported here is to test this hypothesis.

Iron abundances in the neutral Veil are of interest for three other reasons. First, existing depletion data for the ISM suggest a positive correlation between depletion and *mean* gas density along the line-of-sight (see Jenkins 2004). If this trend also applies to *local* gas densities, then depletions in the Veil might be higher than average because the Veil density ($n \approx 10^{2.5-3.5} \text{ cm}^{-3}$, Abel et al. 2004, 2006) is significantly higher than that of the general ISM. Second, Fe abundances in the Veil provide a useful comparison with Fe abundances derived in the Orion H⁺ region. The latter are dependent upon spectral synthesis models, so the comparison between Fe abundances derived for neutral and ionized regions provides a useful check upon the accuracies of the models. Finally, Fe profiles that are very optically thick near line center still provide useful information about outlying velocity components with very low column densities.

In this project we analyze measurements of Fe in the Orion Veil and in other locales along the line of sight to Θ^1 B Orionis. These measurements are based upon archival STIS data which has also been analyzed by Miller et al. (2007). In the data, we identify and analyze Fe I and Fe II absorption lines toward Θ^1 B Ori (§ 4.4, 4.5). We find, as expected, that Fe⁺ is the dominant stage of ionization in the neutral Veil, and we are able to derive accurately the total Fe/H ratio in this layer. We compare our value for Fe/H with previous measurements of this ratio in the main Orion H⁺ region (§ 4.6.1) and consider the implications of this comparison for grain destruction processes. In § 4.6.2, we discuss the connection between Fe abundance and gas density; in § 4.6.3 we consider the implications of the measured Fe/H ratio for spectral synthesis models of the Orion H⁺ region. In § 4.6.4 and 4.6.5 we discuss the nature of outlying velocity components visible in the most optically thick Fe II lines.

4.4. Observational Data

We used archival STIS data originally obtained by Sofia et al. (2004; GO9465) toward Θ^1 B Ori. These data consist of four independent scattered-light corrected spectra (Valenti et al. 2002) that were co-added using IRAF. The data archive numbers are o6lb02010, o6lb02020, o6lb02030, and o6lb02040, all archive data were processed with CalSTIS code version 2.17b prior to our analysis. The coadded spectrum covers the approximate wavelength range 2100 Å to 2500 Å with about 38,000 spectral channels. The channel separation is approximately 0.01 Å. The spectral resolution (FWHM) of the E230H grating is approximately 0.016 Å in this wavelength range, equivalent to 2.1 km s⁻¹. We normalized the coadded spectrum using the IRAF task “continuum” in “ratio” mode over successive 4 Å segments of the spectrum. That is, each 4 Å segment was independently fitted with a linear function, and then the ratio of the data to the fitted function was computed to create a normalized segment (continuum level at unity). The rms noise in the co-added, normalized spectrum is typically 70⁻¹.

We first searched the data with IRAF (Tody, 1993) and identified two Fe I lines and seven Fe II lines. These lines are listed in Table 4.1. All lines, except the Fe I λ 2484 line, were also identified by Miller et al. (2007). Normalized line profiles are shown in Figure 4.3, plotted on the heliocentric velocity scale. ($V_{\text{LSR}} = V_{\text{helio}} - 18.1 \text{ km s}^{-1}$.) The *principal absorption feature* in these profiles lies in the range 11–27 km s⁻¹ (heliocentric). This range is consistent with the results of Abel et al. (2004, 2006), who also considered ultraviolet absorption lines from the Veil. Also visible in the most optically thick lines of

Figure 4.3 are several outlying velocity components with much lower optical depths than the principal absorption feature.

Table 4.1: Properties and Calculated Values of Iron Absorption Lines

λ_{vac} (Å)	Type	Upper level ¹	τ_{peak} observed	τ_{peak} predicted ³	Oscillator strength ⁴	$N \pm \text{error}^6$
2167.4534	Fe I	$4p^5P_3$	0.12	not predicted	0.15	$5.8 \pm 1.1 \times 10^{11}$
2484.0209	Fe I	$4p^5F_5$	0.33	0.18	0.544	$4.5 \pm 0.52 \times 10^{11}$
2234.4472	Fe II	$4p^4F_{7/2}$	0.04	0.08	$2.4 \pm 0.7 \times 10^{-5}$	2.08×10^{15} ⁽⁵⁾
2249.8768	Fe II	$4p^4D_{7/2}$	$2.9^{(2)}$	7.0	0.001821	$2.08 \pm 0.21 \times 10^{15}$
2260.7805	Fe II	$4p^4F_{9/2}$	$3.6^{(2)}$	8.5	0.00244	$2.08 \pm 0.21 \times 10^{15}$
2344.2139	Fe II	$4p^4P_{7/2}$	Undetermined	420	0.1142	Undetermined
2367.5905	Fe II	$4p^4F_{7/2}$	0.23	0.21	$1.2 \pm 0.16 \times 10^{-4}$	2.08×10^{15} ⁽⁵⁾
2374.4612	Fe II	$4p^4F_{9/2}$	Undetermined	110	0.0313	Undetermined
2382.7652	Fe II	$4p^4F_{11/2}$	Undetermined	1200	0.32	Undetermined

¹All transitions are from the ground level.

²Estimated from profiles for which zero level correction $\Delta I_z = -0.01$, see § 4.5.1.

³Predicted from Cloudy spectral synthesis model of Abel et al. (2004) modified to include Fe lines (see § 4.6.3).

⁴Oscillator strengths taken from Morton (2003) and references therein, except for Fe II $\lambda 2234$ and $\lambda 2367$ lines. For these lines, we have derived oscillator strengths empirically as described in § 4.5.2.

⁵No error reported because oscillator strength was scaled so that column density matches the value derived from Fe II $\lambda 2249$ and $\lambda 2260$ lines (see § 4.5.2).

⁶Values reported for Fe II $\lambda 2249$ and $\lambda 2260$ lines are identical since $N(\text{Fe}^+)$ was derived from information about both lines as described in § 4.5.1.

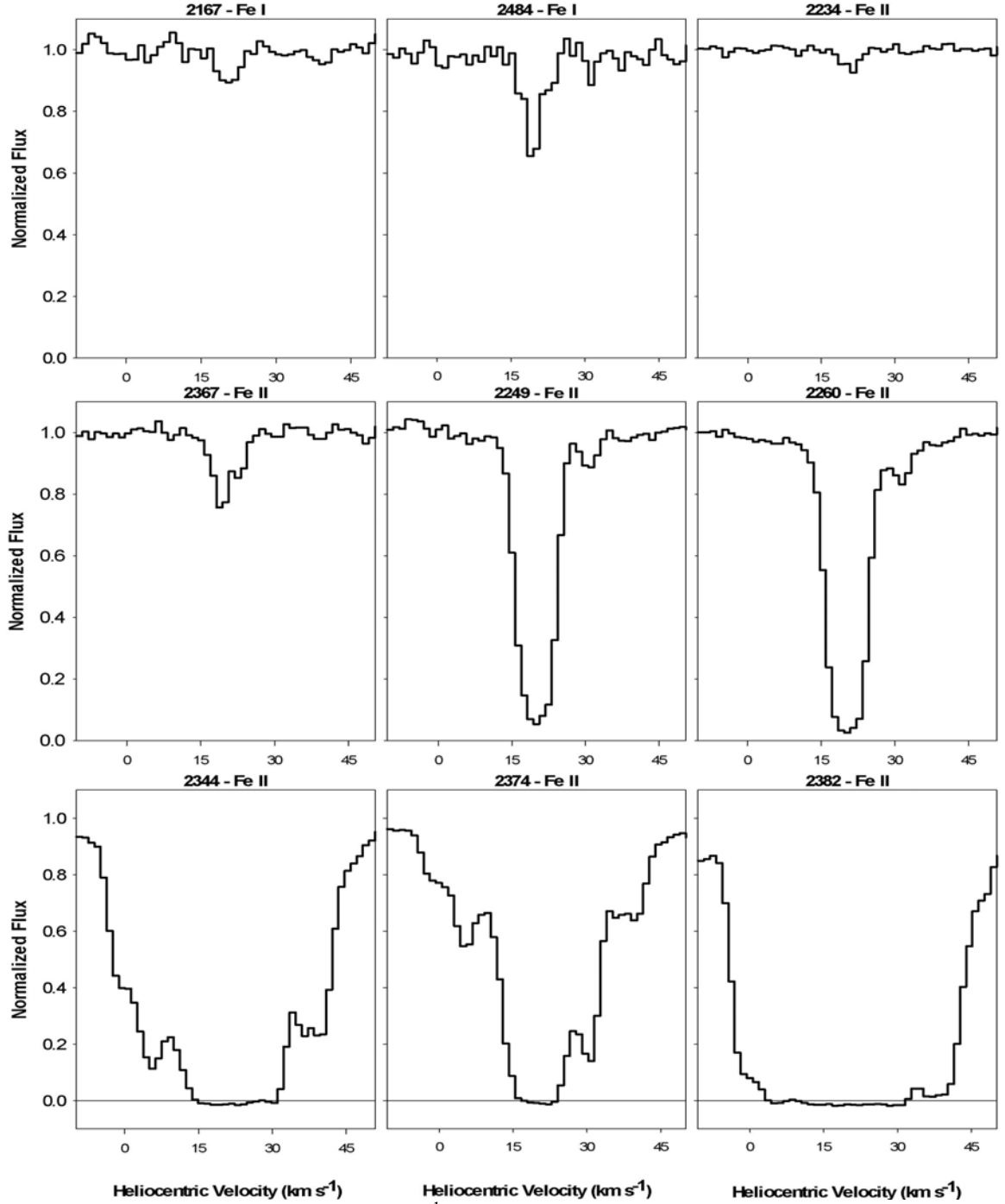


Figure 4.3: Iron absorption lines toward Θ^1 B Orionis. Rest wavelengths are given in angstroms.

4.5. Analysis

Column densities derived from Fe I and Fe II lines should be excellent approximations of *total* column densities of Fe^0 and Fe^+ , respectively. The lower levels of Fe I and Fe II lines in this study are the ground levels for their respective species, $4s^2\ ^5D_4$ for Fe^0 and $4s\ ^6D_{9/2}$ for Fe^+ . The next levels above the ground for these two species

are at $\Delta E/k = 600$ and 550 K, respectively (Fuhr, Martin & Wiese 1988). Since $T_K \approx 100$ K for the Veil (Abel et al., 2006), both Fe^0 and Fe^+ should be overwhelmingly in their ground levels if the excitation is collisional. Moreover, Miller et al. (2007) identified Fe II lines arising from excited level transitions toward Θ^1 B Ori and concluded that $< 1\%$ of Fe^+ is in excited levels. Therefore, column densities derived from the two Fe I lines ($\lambda 2167$ and $\lambda 2484$) provide estimates of $N(\text{Fe}^0)$. Column densities derived from the two moderate optical depth Fe II lines ($\lambda 2249$ and $\lambda 2260$) provide an estimate of $N(\text{Fe}^+)$, subject, as always, to uncertainties in the oscillator strengths.

Oscillator strengths can be experimentally measured in the laboratory, calculated theoretically or estimated empirically from astronomical data. Experimental measurements, where available, provide the most reliable values since they are subject to the fewest assumptions. In the case of the dominant ionization state Fe II lines, oscillator strengths for the low optical depth $\lambda 2234$ and $\lambda 2367$ lines (Figure 4.3) have not been measured experimentally. Miller et al. (2007) review these values and provide a new empirical estimate for the $\lambda 2234$ oscillator strength. Their value is about a factor of 2 smaller than the theoretical value from Morton (2003). Three oscillator strength values are reported in the literature for the $\lambda 2367$ line (including the value adopted by Miller et al.). These values range over a factor of nearly four. In contrast to this situation, oscillator strengths for the moderate optical depth Fe II $\lambda 2249$ and $\lambda 2260$ lines have been measured experimentally to a relative uncertainty of about 8% (Bergeson, Mullman & Lawler 1994). Therefore, these two lines offer the best opportunities to estimate Fe^+ column densities accurately.

4.5.1. Fe column densities derived from optical depth profiles

We used the Fe II $\lambda 2249$ and $\lambda 2260$ lines to estimate $N(\text{Fe}^+)$ by direct integration of the observed optical depth profiles. This technique is commonly used at radio frequencies, and it has also been used at optical wavelengths (*e.g.* Hobbs 1974 and references therein) and in the ultraviolet (*e.g.* Savage & Sembach 1991). We first computed the optical depth profile $\tau_i = -\ln I_i$ for each line from the normalized line profile (I_i), where i is the spectral channel number. The two optical depth profiles are shown in Figure 4.4. Next we calculated $N(\text{Fe}^+)$ using the standard relation

$$N(\text{Fe}^+)_{j,k} = 1.13 \times 10^{20} \frac{\Delta\lambda \sum_k \tau_i}{\lambda_o^2 f} \text{ cm}^{-2}, \quad (37)$$

where λ_o is the rest wavelength in \AA , $\Delta\lambda$ is the channel separation in \AA (0.0093 for the STIS data), and f is the oscillator strength (see Table 4.1). Strictly speaking, equation (37) yields the column density of Fe^+ in its ground level. Channels $j \rightarrow k$ were chosen to include the principal absorption feature only (§ 4.4). However, all outlying velocity components combine to contribute only 5% as much column density as the principal absorption feature (§ 4.6.4 and Table 4.2).

Table 4.2: Parameters of the velocity components

Component	0 (principal)	1	2	3	4
Velocity range (helio)	15 to 25	-8 to 0	0 to 9	26 to 36	36 to 49
$N(\text{Fe})^1$	1.9×10^{15}	6.5×10^{12}	2.0×10^{13}	5.0×10^{13}	1.6×10^{13}
$N(\text{H})^2$	4.8×10^{21}	1.5×10^{19}	4.5×10^{19}	1.1×10^{20}	3.6×10^{19}
A_v^3	1.6	0.008	0.023	0.055	0.018
T_{min} (K)	n/a	n/a ⁴	100	750	250
$N(\text{Ca}^+)$	5.5×10^{11}	3.2×10^{10}	2.8×10^{11}	5.0×10^{11}	1.5×10^{11}
$N(\text{Na}^0)$	1.7×10^{12}	≈ 0	2.7×10^{11}	1.3×10^{11}	≈ 0
$\log(\text{Ca}^+/\text{Fe})$	-3.8	-2.3	-1.9	-2.0	-2.0
$\log(\text{Na}^0/\text{Fe})$	-3.3		-1.9	-2.6	
$\log(\text{Ca}^+/\text{Na}^0)$	-0.49		0.02	0.58	

¹Assumes $N(\text{Fe}) \approx N(\text{Fe}^+)$ since Fe^+ is the principal ionization state and excited states are expected to be very weakly populated (§ 3).

²Assumes $N(\text{Fe})/N(\text{H}) = 4.4 \times 10^{-7}$, as derived for the principal absorption feature of the Veil. For the principal absorption feature, we take $N(\text{H}) = 4.8 \times 10^{21} \text{ cm}^{-2}$, see Abel et al. (2006).

³Assumes average interstellar value $A_v = 5 \times 10^{-22} N(\text{H})$ for components 1-4. Value for principal absorption feature (0) is taken from O'Dell & Yusef-Zadeh (2000).

⁴21 cm optical depth data do not cover this component.

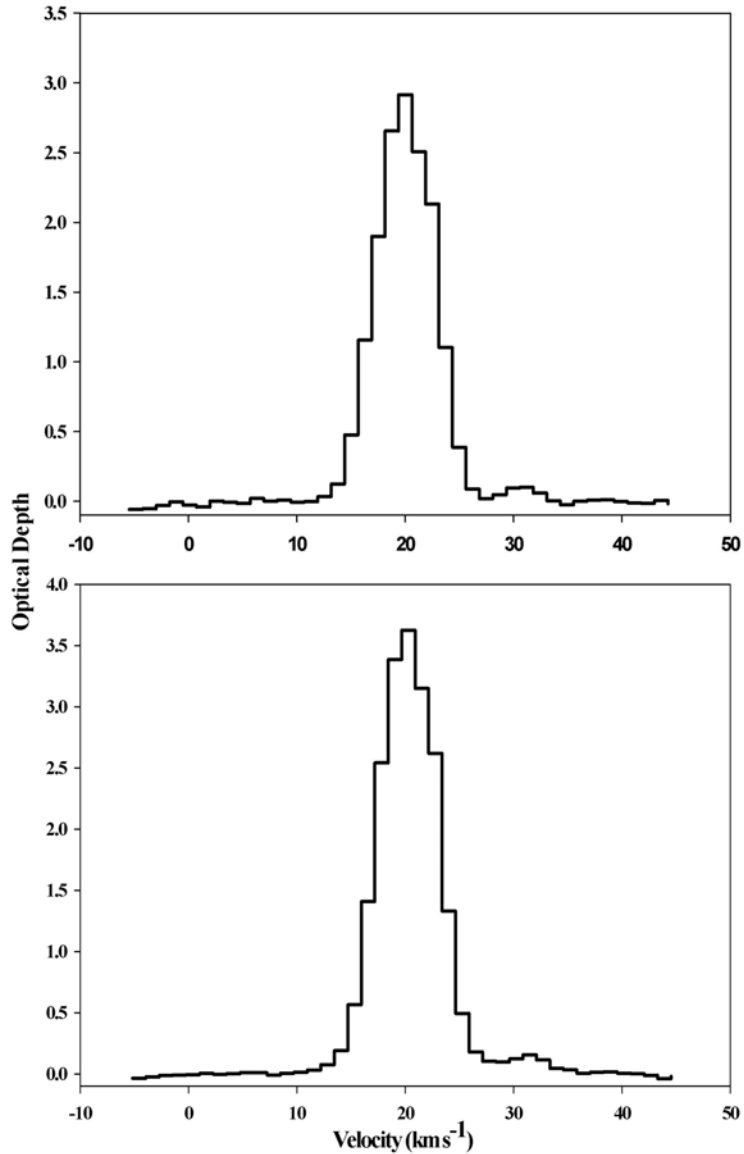


Figure 4.4: Optical depth profiles of the 2249 (top) and 2260 Å (bottom) lines toward Θ^1 B Orionis. Velocities are heliocentric.

Equation (37) is valid for all optical depths as long as the optical depth profile is adequately resolved by the spectrometer, and all values of τ_i are measured (i.e. non-zero signal in each spectral channel). See Savage & Sembach 1996. In practice, there are several sources of uncertainty. Obvious examples are errors in the measured oscillator strengths which we have included in the error calculation. However, other errors can be important. One consideration is the normalization process. Values of I_i will be incorrect if the continuum level is not unity, a problem that affects low optical depth lines especially. Examination of the continuum levels in the spectral vicinities of the $\lambda 2249$ and $\lambda 2260$ lines suggests that the continuum level is very well determined and is unity to within 0.5% and 2% for the two lines, respectively. Therefore, errors in I_i arising from normalization errors are of this order at most, much smaller than the errors in the

oscillator strengths for these two lines. A second consideration is instrumental sensitivity in the high optical depth channels. Specifically, does the STIS spectrum actually detect flux I_i in the most optically thick channels of the two Fe II lines? First we note that in the less optically thick $\lambda 2249$ line, $I_i = 0.043$ at the most optically thick channel, a value 2.7 times larger than the rms in the line-free regions of the adjacent continuum. Therefore, we appear to have detected light at nearly the $3\text{-}\sigma$ level even in this channel. Next, the $\lambda 2249$ and the $\lambda 2260$ optical depth profiles (Fig. 2) are very similar in shape, despite the fact that the theoretical optical depth ratio $f\lambda_{2260}/f\lambda_{2249} = 1.35$. We conclude that instrumental sensitivity has not contributed significantly to errors in the optical depth profiles for these two lines.

Next we consider the effects of inaccurate background subtraction, a particular problem for high optical depth lines like Fe II $\lambda 2249$ and $\lambda 2260$. Background subtraction errors lead to errors in the zero level. As a result, the normalized flux of a spectral channel with infinite optical depth is not zero, as expected, it is ΔI_z . This effect is easily recognized in very high optical depth absorption lines such as the $\lambda 2344$, 2374 and 2382 Fe II lines (Figure 4.3). The flat parts of the normalized line profiles have ΔI_z as much as -0.015 . Zero level errors also affect intermediate optical depth lines such as Fe II $\lambda 2249$ and $\lambda 2260$ for which the calculated optical depths will be in error. We know that zero level errors exist in STIS data in the very high optical depth lines. These errors exist despite the fact that the data were processed by the two dimensional background subtraction algorithm (sc2d). Valenti et al. (2002) plot ΔI_z in high optical depth line cores at selected wavelengths (their Fig. 16, see, also, STIS Instrument Handbook for Cycle 17, fig. 13.97). Values of ΔI_z for E230H grating data processed with the sc2d algorithm are shown in this plot for several wavelengths between about $\lambda 1670$ and 2800 . All values are negative, ranging from about -0.003 to -0.013 . No data exist in the Valenti et al. figure for the Fe II $\lambda 2249$ and $\lambda 2260$ lines. However, it seems reasonable to suppose that $\Delta I_z \neq 0$ at these wavelengths, too. Given the ΔI_z range in the figure of Valenti et al., and the existence of ΔI_z as much as -0.015 in our three very heavily saturated Fe II lines near $\lambda 2330$, we set the range of possible ΔI_z for the Fe II $\lambda 2249$ and $\lambda 2260$ lines at -0.005 to -0.015 . We examine the quantitative consequences of this ΔI_z range below, after considering one additional source of error.

Jenkins (1996) has discussed the effects of spectrally unresolved, optically thick velocity components on optical depth profiles such as those for the Fe II $\lambda 2249$ and $\lambda 2260$ lines. For such a pair of lines, the signature of unresolved velocity components is optical depth ratios across the lines less than the ratio of $f\lambda$ of the two lines. In the present case, $f\lambda_{2260}/f\lambda_{2249} = 1.35 \pm 0.15$, given the experimentally measured oscillator strengths and their uncertainties (see above). Therefore, if the observed optical depth ratios across the two Fe II lines are less than this ratio, saturation owing to unresolved velocity components is presumed to exist. In this case, Jenkins provides an empirical technique to calculate channel-by-channel correction factors $C_i > 1$ as a function of the line ratio $R_i \equiv \tau_{i,2260}/\tau_{i,2249}$, where $1.0 < R_i < 1.35$. The factors C_i are used to scale up the weaker line (i.e. $\lambda 2249$) optical depth profile to correct for saturation effects. We have calculated values of C_i across the line on a spectral channel-by-channel basis. However, the resulting values were not always physically meaningful since for some spectral channels R_i lies outside the allowed range 1.0 to 1.35, perhaps owing to measurement

error. Therefore, we have computed a single value $\langle C \rangle$ based upon the value of R averaged over the central 7 channels of the profiles for which optical depths are of order or greater than 0.5. We then apply $\langle C \rangle$ to the Fe II $\lambda 2249$ optical depth profile from which we compute $N(\text{Fe}^+)$.

We now return to the issue of background subtraction errors and derive a most probable value of $N(\text{Fe}^+)$ from the Fe II $\lambda 2249$ and $\lambda 2260$ line data. We have experimented with correcting the Fe II $\lambda 2249$ and $\lambda 2260$ normalized absorption line profiles for $\Delta I_z = -0.005$ and -0.015 . These corrections reduce the apparent R_i increasingly below the theoretical ratio 1.35. Therefore, the corrections imply increasing (but still modest) effects of spectrally unresolved line components, and higher values of the Jenkins correction ($\langle C \rangle = 1.13$ and 1.22 for $\Delta I_z = -0.005$ and -0.015 , respectively). Next, we derive $N(\text{Fe}^+)$ from Jenkins-corrected Fe II $\lambda 2249$ optical depth profiles, separately for the two values of ΔI_z . The results are $N(\text{Fe}^+) = 2.04 \pm 0.16 \times 10^{15}$ and $2.12 \pm 0.17 \times 10^{15} \text{ cm}^{-2}$ for $\Delta I_z = -0.005$ and -0.015 , respectively. These values for $N(\text{Fe}^+)$ only differ by about 0.5σ . Finally, we take the average of these two values for $N(\text{Fe}^+)$ as the most probable value. For the error in this average, we take one half of the total range of values implied by the two $N(\text{Fe}^+)$ values plus their errors. The result is $N(\text{Fe}^+) = 2.08 \pm 0.21 \times 10^{15} \text{ cm}^{-2}$ (Table 1). This most probable value of $N(\text{Fe}^+)$, assuming the specified range of ΔI_z and applying the Jenkins correction, is only a factor 1.12 higher than we would have computed absent any zero level correction or Jenkins correction. In short, neither the zero level errors (within the assumed range) nor the effects of spectrally unresolved line components has a significant effect upon $N(\text{Fe}^+)$.

We conclude that the most accurate method to measure $N(\text{Fe}^+)$ toward Θ^1 B Ori is direct integration of the $\lambda 2249$ and $\lambda 2260$ optical depth profiles, even considering the errors described above. This method is preferred over direct integration of the weaker $\lambda 2234$ and $\lambda 2367$ profiles for three reasons. First, the $\lambda 2249$ and $\lambda 2260$ oscillator strengths are accurately known from experimental measurement, unlike the oscillator strengths for the two weaker lines. Second, the $\lambda 2249$ and $\lambda 2260$ lines are much stronger, so their integrated optical depths can be determined much more accurately. Third, as discussed above, the effects of unresolved velocity components are small.

We also estimate $N(\text{Fe}^0)$ from the $\lambda 2167$ and $\lambda 2484$ Fe I lines, using the same method of optical depth integration. However, zero level offsets and saturation should have little influence upon these low optical depth lines, so we have ignored these issues. Results are shown in Table 4.1.

4.5.2. New oscillator strength estimates for 2234 & 2367 Å Fe II lines

Given a value of $N(\text{Fe}^+)$ derived from the Fe II $\lambda 2249$ and $\lambda 2260$ lines, we can estimate empirically the oscillator strengths for the weaker Fe II $\lambda 2234$ and $\lambda 2367$ lines. To do so, we insert the integrated optical depth for each line into equation (37) as well as $N(\text{Fe}^+)$ and solve for f . In practice, we compute each oscillator strength and its error from the two previously-derived values of $N(\text{Fe}^+)$, assuming $\Delta I_z = -0.005$ and -0.015 (see above). The most probable value for f_{2234} then becomes the average of the two values of f_{2234} computed from the two values of $N(\text{Fe}^+)$. The error is one half the total range of f_{2234} implied by the two values of f_{2234} and their individual errors. We used the analogous process to find the most probable value of f_{2367} and its error. The results are $f_{2234} = 2.43 \pm$

0.72×10^{-5} and $f_{2367} = 1.21 \pm 0.16 \times 10^{-4}$ (Table 4.1). These two oscillator strengths are higher than those cited by Miller et al. (2007) by factors of 1.9 and 1.5 for the $\lambda 2234$ and the $\lambda 2367$ lines, respectively. We believe that our oscillator strength values are likely to be more accurate. Our values are based upon a simple scaling argument tied to experimentally measured oscillator strengths.

4.5.3. Fe column densities and the Fe/H ratio in the Orion Veil

Data from Table 4.1 allow us to estimate several relevant parameters for the Θ^1 B Ori line of sight through the neutral Veil. One parameter is the ionization ratio Fe^+/Fe^0 . We take the most probable value of $N(\text{Fe}^+)$ from § 4.5.1, and we combine the two values of $N(\text{Fe}^0)$ from Table 4.1 to get $N(\text{Fe}^0) = 5.2 \pm 0.57 \times 10^{11}$. Therefore, $(\text{Fe}^+/\text{Fe}^0) = 4.0 \pm 0.6 \times 10^3$, establishing, as expected, that Fe^+ is the dominant ionization stage in the Veil. Finally, we take the Ly- α based value for $\log N(\text{H}^0) = 21.68 \pm 0.12$ (STIS data, Cartledge et al. 2001) to derive $\log (\text{Fe}^+/\text{H}^0) = -6.36 \pm 0.13$, that is, $\text{Fe}^+/\text{H}^0 = 4.4 \pm 1.3 \times 10^{-7}$. This ratio is a very close approximation to the total ratio Fe/H in the Veil. Fe^+ is the dominant ionization stage, and the Θ^1 B Ori line of sight through the Veil is overwhelmingly atomic, with $N(\text{H}_2)/N(\text{H}^0) \approx 10^{-7}$ (Abel et al. 2006). In principle, Fe^+ can also exist in ionized gas since its ionization potential (16.2 eV) exceeds that of H. Could the measured value $N(\text{Fe}^+)$ include a significant contribution from ionized gas associated with the Veil? The answer is almost certainly no. Abel et al. (2006) consider H^+ associated with the Veil (i.e. H^+ lying on the *near* side of the Trapezium stars). They conclude that this gas is blue shifted by $\approx 15 \text{ km s}^{-1}$ with respect to the Veil. That is, the ionized layer that protects the neutral Veil from ionization by the Trapezium stars lies at a significantly different velocity from the Veil itself, a velocity where Fe II absorption is not detected.

If $\log (\text{Fe}/\text{H}) = -4.55 \pm 0.05$ for the Sun (Asplund, Grevesse & Sauval 2005), then the log of the Veil Fe depletion relative to the Sun is -1.81 ± 0.13 . (See Jensen & Snow 2007 for a discussion of the cosmic value of Fe/H.) Note that the present value for Fe^+/H^0 is larger by about a factor of three than the value of 1.3×10^{-7} reported by Shuping and Snow (1997) toward Θ^1 C Ori. This difference could reflect a real difference along the lines of sight to Θ^1 B and Θ^1 C Ori. More likely, we suspect, the difference reflects uncertainties arising from limitations in the sensitivity and spectral resolution of the IUE data used by Shuping & Snow.

4.6. Discussion

4.6.1. Fe/H in the Orion Veil: Implications for grain destruction

Differences in Fe/H in ionized vs. neutral gas, if present, have implications for grain destruction processes. Our ratio Fe/H in the Orion neutral Veil ($4.4 \pm 1.3 \times 10^{-7}$, § 4.5.3) is quite consistent with the results of Rodriguez & Rubin (2005) for the Orion H^+ region ($5\text{--}12 \times 10^{-7}$), and it is quite comparable with the range $6.8\text{--}9.4 \times 10^{-7}$ obtained for the Orion H^+ region by Esteban et al. (2004). However, these results also allow Fe/H to be as much as a factor of two higher in the H^+ gas. If so, then grain material may have been destroyed in the ionized gas, leading to an enhanced gaseous Fe concentration relative to the neutral gas.

We have estimated the fraction of grain mass F_{gr} that would be destroyed in the H^+ gas in order to increase the gas phase Fe abundance by a factor of two. To make this estimate, we assumed the grain chemical abundances of Zubko, Dwek & Arendt (2004). These abundances (their Table 1) imply that total grain mass amounts to 1% of H mass, and that Fe accounts for 15% of the grain mass. To estimate F_{gr} , we also made use of the ratio Fe^+/H^0 derived above for the Veil. We find that gas phase Fe is increased by a factor of two in the H^+ gas if only 1.5% of the grain material is destroyed (i.e. returned to the gaseous state). We conclude that no more than a very small fraction ($< 2\%$) of grain mass has been destroyed in the Orion H^+ gas. That is, grain destruction in H^+ regions is insignificant, at least in the Orion H^+ region, despite the correlation between Fe abundance and the degree of ionization in H^+ regions reported by Rodriguez (2002). This result is consistent with the idea that Fe in grains lies within resilient grain cores (Jenkins 2004), and it is unlikely to be released in to the gas phase in H^+ regions. (Also, see Osterbrock 1989.) Moreover, Ca is highly depleted in the Orion H^+ region (Kingdon, Ferland & Feibelman 1995), a clear indication that refractory grain material lies mostly within the grains in the ionized gas.

4.6.2. Fe/H in the Orion Veil: the depletion – density relation

Apart from the implications for grain destruction processes, the Fe abundance in the Orion Veil is of interest for another reason. The Veil density (§ 4.3) is an order of magnitude (or more) higher than densities expected in typical diffuse clouds of the cold neutral medium (CNM). Densities in the CNM are of order $50\text{-}100\text{ cm}^{-3}$; densities in warm neutral material (WNM) are more than an order of a magnitude lower. (See Heiles & Troland (2003).) Moreover, indications exist that depletions are sensitive to physical conditions in the ISM. (See review by Jenkins 2004.) Jenkins, Savage & Spitzer (1986) discovered a positive correlation between the depletion of many elements and the mean density along the line of sight $\langle n_{\text{H}} \rangle$. Included among these elements is Fe. They interpreted this phenomenon in terms of a two phase ISM model of Spitzer (1985). In this model, depletions are lower in warmer, lower density material (likely the WNM in current terms), and they are higher in colder, denser material (likely the CNM). The value of $\langle n_{\text{H}} \rangle$ is seen as a proxy for the proportion of CNM to WNM along a given line of sight, with higher values of $\langle n_{\text{H}} \rangle$ an indication of a greater proportion of CNM. The depletion – density relation has been further studied by others, among them Cartledge et al. (2004) for O/H and Jensen & Snow (2007) for Fe/H. Both of these groups report a tendency toward two discrete depletion values, with the O/H ratio decreasing by about 0.14 dex for $\langle n_{\text{H}} \rangle$ higher than about 1.5 cm^{-3} , and the Fe/H ratio decreasing by about 0.5 dex above a similar value for $\langle n_{\text{H}} \rangle$. However, the density-depletion relation reported by Jensen & Snow (2007) and other authors is based upon *averages* of both parameters along lines of sight to stars. It is not known, for example, if lines of sight with higher $\langle n_{\text{H}} \rangle$ are also lines of sight with higher local densities. To better understand the density-depletion relationship, data are needed on these parameters in localized regions of the ISM.

What is the relevance of the Orion Veil Fe/H ratio to the density-depletion question? Along the Veil line of sight, $\langle n_{\text{H}} \rangle \approx 3\text{ cm}^{-3}$. Therefore, the Veil density falls within the regime of statistically higher depletions (i.e. lower ratios Fe/H) in the data of Jensen & Snow (2007, see their Fig. 6). However, the measured Veil ratio Fe/H is more consistent

with the regime of *lower* depletions (i.e. higher ratios Fe/H). That is, the Veil line of sight is not consistent with the overall trend of Fe/H vs. $\langle n_H \rangle$ as reported by Jensen & Snow (2007). (We note that there are several other discrepant points in the Fe/H vs. $\langle n_H \rangle$ data of these authors.) The real significance of the Veil Fe/H ratio is the fact that the *local* density and Fe depletion in the sampled region are both known, and the density is quite high ($n_H \approx 10^3 \text{ cm}^{-3}$, § 4.3). Therefore, the Veil result suggests that depletion does not increase with local density, at least for $n_H \leq 10^3 \text{ cm}^{-3}$. It is possible that lines of sight studied by Jensen & Snow (2007) with higher $\langle n_H \rangle$ (and higher depletions) have $n_H > 10^3 \text{ cm}^{-3}$ in localized regions. These localized regions might be translucent molecular clouds rather than more common and lower density CNM. Alternately, physical conditions other than local density may be important in controlling depletion. For example, the WNM may be more subject to grain-destroying shocks, or else grain growth may be inhibited at the higher temperatures of WNM. Further investigation of the depletion – density relation would be greatly assisted by more measurements of these two parameters in localized regions of the ISM.

4.6.3. Comparisons with spectral synthesis models of the Orion region

Under suitable circumstances, absorption line column densities are subject to relatively few uncertainties (§ 4.5.1). In contrast, emission line column densities require a spectral synthesis model to calculate temperature-dependent effects upon the emission line intensities and to provide ionization correction factors if the observed lines do not originate from the dominant ionization state. See, for example, Baldwin et al. (1991), Rubin et al. (1997), Ferland (2003), and Rodriguez & Rubin (2005). Since emission line column density estimates are so model dependent, it is important to have observational constraints upon the models. Our results for the Veil provide such a constraint. In particular, the similarity in derived ratios Fe/H for the Veil and for the main Orion H⁺ region (§ 4.6.1) strongly suggests that the H⁺ region models of Rodriguez & Rubin are at least approximately correct. This conclusion, of course, is dependent upon the assumption that little or no iron has been released into the gas phase in the H⁺ region.

As a further comparison between observations and models, we have rerun the spectral synthesis model of Abel et al. (2004) for the neutral Veil, now including the Fe line predictions (Verner et al. 1999). In rerunning this model, we used the observed $N(\text{Fe})$ from the present work and the STIS-derived value for $N(\text{H}^0)$ from Cartledge et al. (2001). We also assumed the STIS-derived b -value of 3 km s^{-1} to compute predicted optical depths of the Fe I and Fe II lines given in Table 4.1. The predicted peak optical depths match the observed peak optical depths quite well, usually to about a factor 2 or better, see Table 4.1. Finally, the Abel et al. Veil model predicts $\log \text{Fe}^+/\text{Fe}^0 = 3.7$, similar to the observed value 3.6 from the present work. This agreement lends further confidence to the Abel et al. (2004) model, especially to its prediction of the Veil position 1-3 pc in front of the principal ionizing star $\Theta^1\text{C Ori}$.

4.6.4. Outlying velocity components

Inspection of the most optically thick Fe II line profiles in Figure 4.3 reveals several weaker velocity components that are red-shifted and blue-shifted from the principal absorption feature. These components are spread over the approximate range -7

to 48 km s⁻¹ heliocentric. They match quite well with velocity components in high spectral resolution Ca II and Na I optical absorption spectra of the Trapezium stars (Hobbs 1978, O'Dell et al. 1993, and Price et al. 2001). While the total velocity range of the outlying Fe components is rather wide, this range, nonetheless, falls within the range covered by 21 cm HI emission from the Orion region (Green 1991). In this sense, there is nothing anomalous about the velocity range covered by the outlying Fe components.

We have identified four velocity intervals outside the main Fe component. Each interval approximately encompasses a velocity component also present in the Ca II and Na I optical absorption lines. These velocity ranges are given in Table 4.2, and they are numbered one through four. Within each velocity interval, we estimate $N(\text{Fe}^+)$ from the $\lambda 2374$ line optical depth profile, using the equation and procedures of § 4.5.1. Results are shown in Table 4.2 for each of the four outlying velocity intervals. We have converted $N(\text{Fe})$ in each velocity interval to $N(\text{H})$, using the ratio Fe/H derived for the principal absorption feature. These values are also given in Table 4.2 along with the corresponding values of A_v . For completeness, we have also provided parameters in Table 4.2 for the principal absorption feature (labeled 0 in Table 4.2). Estimates of $N(\text{H})$ for the outlying velocity components are the first reliable values to be determined. Although previous optical profiles of the Ca II and Na I lines revealed the existence of these velocity components, it is difficult to derive $N(\text{H})$ from the optical profiles because they sample trace stages of ionization (see Abel et al. 2004). Note, however, our assumption that Fe/H is the same in the outlying velocity components as it is in the main component is not necessarily correct. As discussed in § 4.6.2, the ratio Fe/H is observed to vary by at least 0.5 dex, with higher values (i.e. lower depletions) associated with lines of sight having lower mean densities (Jensen & Snow 2007). It is possible, therefore, that Fe/H is higher in the outlying velocity components by as much as 0.5 dex. In this case, $N(\text{H})$ estimated for these components could be as much as 0.5 dex lower than the values in Table 4.2.

Table 4.2 also lists other parameters of the outlying velocity components. We have estimated $N(\text{Ca}^+)$ and $N(\text{Na}^0)$ for each of the outlying velocity intervals from the profiles of Price et al. (2001) toward $\Theta^1\text{C Ori}$. We take these profiles as representative of those toward the $\Theta^1\text{B Ori}$ line of sight since the lower spectral resolution Ca II profiles of O'Dell et al. 1993 are very similar for $\Theta^1\text{B Ori}$ and $\Theta^1\text{C Ori}$. Also, the VLA 21 cm HI opacity profile (Abel et al. 2004) toward the Trapezium stars shows no sign of absorption from outlying velocity intervals 2 through 4. (Velocity interval 1 is outside the VLA bandpass of the observation.) On this basis, we can set lower limits to the 21 cm spin temperature T_s for these three velocity components where T_s should be a reasonable approximation to the kinetic temperature T_K . These minimum temperatures are also listed in Table 4.2. They are based upon the values of $N(\text{H})$ in the table which, in turn, assume a common ratio Fe/H in all absorption components. As discussed above, the ratio Fe/H might be as much as 0.5 dex higher in the outlying velocity components. In such a case, the minimum temperatures could also be as much as 0.5 dex higher than the values given in Table 4.2.

4.6.5. Physical nature of the outlying velocity components

O'Dell et al. (1993) and Price et al. (2001) developed models for the locations of Ca II, Na I and other velocity features toward Orion. In this regard, it is important to

recognize that the outlying velocity components need not be related to the Orion complex, they could be small concentrations of ISM anywhere along the line of sight to Orion. Indeed, Welty, Morton & Hobbs (1996) and Welty, Hobbs & Kulkarni (1994) observed Na I and Ca II absorption lines, respectively, toward a large number of stars, sampling a variety of lines-of-sight. Most profiles reveal numerous velocity features, strongly suggesting that Ca^+ and Na^0 absorption arises commonly in the general ISM.

The physical nature of the outlying velocity components is constrained by their parameters listed in Table 4.2. First, these components have small column densities with $N(\text{H})$ typically $\approx 10^{19} \text{ cm}^{-2}$. If they are regions of CNM, then they lie toward the lower end of the CNM column density distribution reported by Heiles & Troland (2003). Second, values for $\log(\text{Ca}^+/\text{Fe})$ in Table 4.2 show a distinct difference between the principal absorption feature (-3.8) and the outlying velocity components (≈ -2). That is, the ratio Ca^+/Fe is nearly two orders of magnitude higher in the outlying velocity components than in the principal absorption feature from the Veil. This difference could be the result of lower ionization levels in the outlying components or of higher ratios Ca/Fe or both.

If the outlying velocity components are far removed from the Trapezium region, they will be in lower ionization levels than the principal Veil absorption feature. In the Veil model of Abel et al. (2004), Ca^{++} is the principal ionization stage, Ca^+ is the secondary stage ($\text{Ca}^+/\text{Ca}^{++} \approx 10^{-2}$). All other ionization stages are at least three orders of magnitude less abundant than Ca^+ . Therefore, lower levels of ionization are characterized by higher abundances of Ca^+ at the expense of recombining Ca^{++} . Ionization level is controlled by the balance between ionizations and recombinations, proportional, respectively, to the ionizing flux and the square of the density. For a single source of stellar ionizing radiation, we expect $\text{Ca}^+/\text{Ca}^{++} \approx \text{Ca}^+/\text{Ca}$ to be proportional to $r^2 n^2$, where r is the distance to the ionizing star and n is the density. Assume, for example, that the outlying components are intervening CNM, and they have n an order of magnitude lower than n in the principal Veil absorption feature. If the Ca^+/Ca ratio is also two orders of magnitude higher in the outlying components, then these components must lie 100 times as far from the ionizing source (Trapezium stars) as the Veil, or about 200 pc away. We conclude that the high measured values of Ca^+/Fe in the outlying components can be explained as a result of the low Ca ionization level, assuming these components lie far from the ionizing stars.

If not an effect of lower ionization level, the higher measured Ca^+/Fe in the outlying velocity components could result from enhancements in Ca/Fe . Such enhancements, in turn could come from differences in the depletions of Ca and Fe. Crinklaw, Federman & Joseph (1994) find that the depletion of Ca is a stronger function of mean line-of-sight density than the depletion of Fe. Since the outlying velocity components likely have lower n than the principal feature, it is possible that depletion of Ca is less relative to Fe in the outlying components. If so, then Ca would be more abundant relative to Fe in these regions. How important is differential depletion in determining Ca^+/Fe , relative to the effects of lower ionization level? We cannot know for sure. However, it seems unlikely that the full two orders of magnitude enhancement in observed Ca^+/Fe in the outlying velocity components comes only from differential depletion effects. Suppose, for example, that differential depletion and ionization balance each account for an order of magnitude increase in Ca^+/Fe in the outlying components.

Then, by the argument given above, the outlying components would still be about 30 times as far from the Trapezium stars as the Veil, or about 60 pc away.

The most likely scenario for the outlying velocity components is that they originate well in front of the Trapezium stars, and they are unrelated to the Orion region. Instead, they are likely to reside somewhere in the Local Bubble of generally hot, low density gas that extends away from the Sun to the general region of Orion (Frisch & York 1983; Heiles 1998). Both in terms of $N(\text{H})$ and velocity widths, the outlying components fall well within the range of values found by Heiles & Troland (2003) for the CNM. The lower limits upon temperature of Table 4.2 also fall within the range of measured temperatures in the CNM by Heiles & Troland (2003). Finally, the ratio Na^0/Fe is also higher in the two outlying components where the Na I line is detected than in the principal Veil absorption feature (Table 4.2). This circumstance may be another indication that outlying components are in lower states of ionization owing to their greater distances from the Trapezium stars.

Another line of evidence suggests that the outlying velocity components arise in gas that is not directly related to the Veil. $N(\text{H}) = 2.4 \times 10^{20} \text{ cm}^{-2}$ for these components combined (Table 4.2). This value is very similar to the value $1.4 \times 10^{20} \text{ cm}^{-2}$ reported by Meyer et al. (1994) for the line of sight to ι Ori. This star lies about $30'$ south of the Orion Nebula, and its line of sight is unlikely to pass through the Veil. Therefore, the line to sight to ι Ori most likely samples the general ISM between us and the Orion region, the same region sampled by the outlying velocity components in Fe II lines along the line of sight to $\Theta^1\text{B Ori}$.

4.7. Conclusions

This study reports a very accurate determination of the gas phase Fe abundance in the neutral Veil of Orion where $n \approx 10^{2.5-3.5} \text{ cm}^{-3}$. For the Veil (i.e. the principal absorption feature), we find $N(\text{Fe}^+) = 2.08 \pm 0.21 \times 10^{15} \text{ cm}^{-2}$. Since Fe^+ is by far the dominant ionization state (§ 4.5.3) and since less than 1% of Fe^+ is in excited levels (§ 4.5), our measurement of $N(\text{Fe}^+)$ with its error applies equally well to the total $N(\text{Fe})$ in the Veil. Moreover, our determination of $N(\text{Fe}^+)$ from the $\lambda 2249$ and $\lambda 2260$ lines allows us to calculate the oscillator strengths for the weaker $\lambda 2234$ and $\lambda 2367 \text{ \AA}$ Fe II lines in a straightforward way. These values are given in Table 4.3.

We estimate the ratio Fe/H in the neutral Orion Veil by combining our value of $N(\text{Fe})$ with the value for $N(\text{H}^0)$ of Cartledge et al. (2001), both of which apply to the line to sight to $\Theta^1\text{B Ori}$. This ratio ($4.4 \pm 1.3 \times 10^{-7}$, § 4.5.3) is quite consistent with previous determinations of this ratio for the Orion H^+ region (§ 4.6.1), although it is about a factor of three higher than the Shuping & Snow (1997) value for the Veil. However, the latter estimate is based in part upon high optical depth, spectrally unresolved Fe II lines observed with IUE from which accurate column densities are more difficult to estimate. The consistency between the new Fe/H ratio derived for the Veil and the previously derived values for the H^+ region may be interpreted in two opposite ways. First, the consistency may be taken as an indication that grain destruction in the H^+ region (if any) has not released an appreciable amount of Fe into the gaseous state, consistent with grain destruction theory. Alternately, if one assumes in advance that grains have not been destroyed in the Orion H^+ region, then the consistency of Fe/H ratios in neutral and ionized gas indicates that spectral synthesis models of the latter are accurate. Finally, the

measured Fe/H in the Veil shows no indication of enhanced depletion despite that fact that the Veil is denser than most ISM (e.g. CNM) along lines of sight to stars. We infer that if depletion is enhanced in higher density regions, as some studies have suggested, then this enhancement does not begin until densities exceed the Veil density $n_{\text{H}} \approx 10^3 \text{ cm}^{-3}$.

In addition to the principal Fe absorption feature, there are several other outlying components visible in the spectra of Figure 4.3. We have estimated $N(\text{Fe})$ for these components from Fe II line profiles that are very optically thick in the principal Veil absorption feature. Also, we have estimated $N(\text{H})$ in these outlying components from the ratio Fe/H derived from the principal absorption feature. We find that the outlying components have low column densities ($N(\text{H}) \approx 10^{19} \text{ cm}^{-2}$). Using previously-published optical Ca II profiles, we derive the ratio Ca^+/Fe for these components, finding that this ratio is nearly two orders of magnitude higher than for the principal absorption feature. We estimate that the higher ratio Ca^+/Fe in the outlying velocity components could arise entirely from a lower ionization level of Ca if the outlying velocity components are far removed from the Trapezium stars. However, a higher ratio Ca/Fe might also apply to the outlying velocity components owing to differential depletion effects. We argue, however, that this latter effect is unlikely to be dominant, and the outlying velocity components are most likely concentrations of CNM lying well in front of the Orion H⁺ region and unrelated to the Orion region.

5. Chapter Five: Conclusions

This document describes studies of two independent regions of the interstellar medium, both of which are associated with active star formation in the Galaxy. In chapter 3 we measured the Zeeman Effect on the 21 cm H I absorption line in order to measure the line of sight magnetic fields in W3. We found that our magnetic field values were consistent in sign with previous results but higher. The primary difference was that we did not find significant detections in the regions south of W3 A and B, referred to as NGC 896. From our magnetic field values we were able to create a three dimensional model of the magnetic field. This model is an hourglass model which is consistent with the previous work of Roberts et al (1993) and Troland (1989). In chapter 2 we used the STIS instrument on the HST to measure the abundance of iron in the neutral region called Orion's Veil. We found that our measurement of the column density of Fe in the Veil is quite consistent with column density measurement in the H⁺ regions near the Veil. We concluded then that it is unlikely that grains in the H⁺ region were destroyed by the photons that ionize that region since there is not a significantly higher amount of Fe in the gas phase in that region than in the Veil. We also concluded that, at least for the Veil, higher density does not produce higher depletion. Using the fact that we had several absorption lines suitable for measuring the column density, we were able to measure the oscillator strengths of two of the transitions where the oscillator strengths were poorly known. Finally, we concluded that the material creating the outlying velocities components must be cold neutral material along the line of sight to the Veil, but it is not related to it.

These two studies provide measurements of some of the fundamental properties of two regions of the ISM. These quantities help us understand the nature of the ISM and its processes. They help us to understand how stars are born and how they affect the environment around them. By understanding star formation, we can how our Sun was born. With future study we may understand why our Sun is not a binary like so many others are and why planets formed around some stars but not others. Once we understand these things, we will have truly solidified the historic link between humans and the ISM.

6. References

- Abel, N. P., Brogan, C. L., Ferland, G. J., O'Dell, C. R., Shaw, G., & Troland, T. H. 2004, *ApJ*, 609, 247
- Abel, N. P., Ferland, G. J., O'Dell, C. R., Shaw, G., & Troland, T. H. 2006, *ApJ*, 644, 344
- Asplund, M., Grevesse, N. & Sauval, A. J. 2005, in *Cosmic Abundances as Records of Stellar Evolution and Nucleosynthesis in honor of David L. Lambert*, A.S.P. Conference Ser., Vol 336, eds. Barnes, T. G., III; Bash, F. N., 25
- Baldwin, J. A., Ferland, G. J., Martin, P. G., Corbin, M. R., Cota, S. A., Peterson, B. M., & Slettebak, A. 1991, *ApJ*, 374, 580
- Bergeson, S.D., Mullman, K.L., & Lawler, J. E. 1994, *ApJ*, 435, L159
- Cartledge, S. I. B., Meyer, D. M., Lauroesch, J. T. & Sofia, U. J. 2001, *ApJ*, 562, 394
- Cartledge, S. I., Lauroesch, J. T., Meyer, D. M., & Sofia, U. J. 2004, *ApJ*, 613, 1037
- Crinklaw, G., Federman, S. R., & Joseph, C. L. 1994, *ApJ*, 424, 748
- Crutcher, R. M. 1999, *ApJ*, 520, 706
- Dickel, H. R., Dickel, J. R., Wilson, W. J., & Werner, M. W. 1980, *ApJ*, 237, 711
- Dickman, R. L. 1978, *ApJS*, 37, 407
- Esteban, C., Peimbert, M., García-Rojas, J., Ruiz, M. T., Peimbert, A., & Rodríguez, M. 2004, *MNRAS*, 355, 229
- Feigelson, E. D. & Townsley, L. K. 2008, *ApJ*, 673, 354
- Ferland, G. J. 2003, *ARAA*, 41, 517
- Frisch, P. C. & York, D. G. 1983, *ApJ*, 271, L59
- Fuhr, J. R., Martin, G. A., & Wiese, W. L. 1988, *J Phys Chem Ref Data*, 17, Supplement 4.
- Fuller, G. A., & Myers, P. C. 1992, *ApJ*, 384, 523
- Garmany, C. D., & Stencel, R. E. 1992, *A&AS*, 94, 211
- Green, D. A. 1991, *MNRAS*, 253, 350
- Heiles, C. & Troland, T. H. 2003, *ApJ*, 586, 1067
- Heiles, C. 1998, *ApJ*, 498, 689
- Hobbs, L. M. 1974, *ApJ*, 191, 381
- Hobbs, L. M. 1978, *ApJS*, 38, 129
- Jenkins, E. B. 1996, *ApJ*, 471, 292
- Jenkins, E. B. 2004, in *Origin and Evolution of the Elements, from the Carnegie Observatories Centennial Symposia*, Carnegie Observatories Astrophysics Series, eds. A. McWilliam and M. Rauch (Cambridge University Press), 336
- Jenkins, E. B., Savage, B. D., & Spitzer, L. 1986, *ApJ*, 301, 355
- Jensen, A. G., & Snow, T. P. 2007, *ApJ*, 669, 378
- Kingdon, J., Ferland, G. J., & Feibelman, W. A. 1995, *ApJ*, 439, 793
- Lada, C. J., Elmegreen, B. G., Cong, H.-I., & Thaddeus, P. 1978, *ApJ*, 226, L39
- McKee, C. F., Zweibel, E. G., Goodman, A. A., & Heiles C. 1993, *Protostars and Planets III*, ed. E.H. Levy & J.I. Lunine (Tucson: Univ. Arizona Press), 327
- Meyer, D., Jura, M., Hawkins, I., & Cardelli, J. 1994, *ApJ*, 437, L59
- Miller, A., Lauroesch, J. T., Sofia, U. J., Cartledge, S. I. B., & Meyer, D. M. 2007, *ApJ*, 659, 441

- Morton, D. C. 2003, *ApJS*, 149, 205
- Mouschovias, T. Ch. & Spitzer, L., Jr. 1976, *ApJ*, 210, 326
- Normandeau, M., Taylor, A. R., & Dewdney, P. E. 1997, *ApJS*, 108, 279
- O'Dell, C. R. 2001, *ARA&A*, 39, 99
- O'Dell, C. R., & Yusef-Zadeh, F. 2000, *AJ*, 120, 382
- O'Dell, C. R., Valk, J. H., Wen, Z., & Meyer, D. M. 1993, *ApJ*, 403, 678
- Oey, M. S., Watson, A. M., Kern, K., & Walth, G. L. 2005, *AJ*, 129, 393
- Ojha, D. K., Tamura, M., Nakajima, Y., et al. 2004, *ApJ*, 608, 797
- Osterbrock, D. E. 1989, *Astrophysics of Gaseous Nebulae and Active Galactic Nuclei* (Mill Valley: University Science Books)
- Price, R. J., Crawford, I. A., Barlow, M. J. & Howarth, I. D. 2001, *MNRAS*, 328, 555
- Roberts, D. A., Crutcher, R. M., & Troland, T. H. 1997, *ApJ*, 479, 318
- Roberts, D. A., Crutcher, R. M., Troland, T. H., & Goss, W. M. 1993, *ApJ*, 412, 675
- Rodriguez, M. & Rubin, R. H. 2005, *ApJ*, 626, 900
- Rodriguez, M. 2002, *A&A*, 389, 556
- Rubin, R. H., Dufour, R. J., Ferland, G. J., Martin, P. G., O'Dell, C. R., Baldwin, J. A., Hester, J. J., Walter, D. K. & Wen, Z. 1997, *ApJ*, 474, L131
- Savage, B. D. & Sembach, K. R. 1991, *ApJ*, 379, 245
- Savage, B. D. & Sembach, K. R. 1996, *ARA&A*, 34, 279
- Shuping, R. Y., & Snow, T. P. 1997, *ApJ*, 480, 272
- Sofia, U. J., Lauroesch, J. T., Meyer, D. M. & Cartledge, S. I. B. 2004, *ApJ*, 605, 272
- Spitzer L., 1998, *Physical Processes in the Interstellar Medium*. Wiley Classics Library, J. Willey & Sons, NY
- Spitzer, L. 1985, *ApJ*, 290, L21
- Thronson, H. A., Jr., Lada, C. J., & Hewagama, T. 1985, *ApJ*, 297, 662
- Tieftrunk, A. R., Gaume, R. A., Claussen, M. J., Wilson, T. L., & Johnston, K. J. 1997, *A&A*, 318, 931
- Tieftrunk, A. R., Megeath, S. T., Wilson, T. L., & Rayner, J. T. 1998, *A&A*, 336, 991
- Tieftrunk, A. R., Wilson, T. L., Steppe, H., et al. 1995, *A&A*, 303, 901
- Tody, D. 1993, in *Astronomical Data Analysis Software and Systems II*, A.S.P. Conference Ser., Vol 52, eds. R.J. Hanisch, R.J.V. Brissenden, & J. Barnes, 173
- Tomisaka, K., Ikeuchi, S., & Nakamura, T. 1988, *ApJ*, 335, 239
- Troland, T. H., Crutcher, R. M., Goss, W. M., & Heiles, C. 1989, *ApJ*, 347, L89
- Valenti, J. A., Lindler, D., Bowers, C., Busko, I., & Quijano, J. K. 2002, *Instrumental Science Report STIS 2002-001*
- Verner, E. M., Verner, D. A., Korista, K. T., Ferguson, J. W., Hamann, F., & Ferland, G. J. 1999, *ApJS*, 120, 101
- Welty, D. E., Hobbs, L. M. & Kulkarni, V. P. 1994, *ApJ*, 436, 152
- Welty, D. E., Morton, D. C., & Hobbs, L. M. 1996, *ApJS*, 106, 533
- Zubko, V., Dwek, E., & Arendt, R. G. 2004, *ApJS*, 152, 211

7. Vita

Biographical Information

Name: Matt Lykins

Date of Birth: April 5th, 1982

Place of Birth: Cincinnati, OH

Professional Preparation

Eastern Kentucky University

Physics

B.S.

2004

University of Kentucky

Physics

M.S.

2007

Appointments

2005-2010

Research Assistant, Radio Astronomy Group,
Dept. of Physics and Astronomy, University of Kentucky,
Lexington, KY

2004-2005

Graduate Teaching Assistant, Dept. of Physics and
Astronomy, University of Kentucky, Lexington, KY

Scholastic and Professional Honors

Recipient, NASA Space Grant Fellowship, Kentucky Space Grant Consortium, 2006-2009

Relevant Publications

Lykins M., Abel N.P., Troland T.; "Physical Conditions in Orion's Veil III:

UV Iron Absorption Lines toward Theta1B Orionis,"; ApJ, accepted 02 Mar 2010

Matt Lykins